

Confirming Mode Identifications using Lightcurve Fitting in DAV G 29-38

Presented by: **Sam D. Barber**

In partial fulfillment of the requirements for graduation with the Dean's
Scholars Honors Degree in Astronomy

Supervisor: **Michael H. Montgomery**

Honors Advisor in Astronomy: **Adam L. Kraus**

April 24, 2023

Abstract

Variable luminosity White Dwarf Giclas 29-38, of spectral type DAV, has been previously observed to have large amplitude pulsation modes of varying frequency and amplitude. Using time series light curve data spanning 23 days from the TESS (Transiting Exoplanet Survey Satellite) spacecraft, we have employed advanced Fourier Transform techniques to extrapolate the individual pulsation modes of the star. These pulsation modes have been compared to past results gathered by Kleinman et al. [1] [2]. A White Dwarf pulsation modeling code, based on the previous work of Montgomery (2005) [3] and Montgomery et al.(2010) [4], was used to independently confirm the ℓ and m values for two pulsation modes determined by Uzundag et al. [5] with varying success. Future study will use observations from the Hubble Space Telescope (HST) to create a model of G 29-38's surface during pulsation events, allowing for the surface composition of different areas of the stellar surface to be estimated.

*There's a really big difference
between trying not to fall and
trying as hard as you can.*

– Elijah Kiser

Acknowledgements

There are so many people that I can thank for where I am today, this list is just the beginning.

First, I have to thank my family, who have graciously supported me and my interest in astronomy my entire life. They've driven hours to find dark skies, listened to countless lectures about faraway galaxies, and helped me find a school where I could continue to pursue my interests. My parents, in particular, have supported my passion for astronomy since I was a toddler on the NASA Kids website, memorizing the moons of Jupiter. My grandparents let me use their house as a home base for observations, and even helped me build telescopes of my own. I will forever be thankful. (P.S. I'm sorry, there aren't many pretty pictures in this paper).

I owe so much to my amazing advisor, Dr. Mike, who has sat through countless silly questions, explained complicated topics over and over, conveyed information in a way that I could understand and actually learn, and listened to a fair bit of baseball talk. I'm honored to have been able to work with such an accomplished scientist and good person.

I would like to thank other members of UT's faculty who have helped me along the way: my advisors, Mark Hemenway and Dr. Adam Kraus, Dr. Caitlin Casey, Dr. Tim Andeen, Dr. Peter Onyisi, Dr. Timothy Perutz, and Dr. Vernita Gordon, among others. I would especially like to thank Joshua Roebke for providing an excellent writing environment and constructive criticism for the writing of this paper.

I have to thank Paul D. Price, my chemistry and physics teacher in high school, for preparing me for my experience in college and encouraging me to learn and understand as much as I could about the universe. I would not be where I am today without him. Lastly, I would like to thank my friends, who have kept me (mostly) sane throughout this whole thing. Special thanks go out to Henry Long, Ignacio Perez, Owen Sabolcik, Shruti Sahu, and Luisa Dalton.

Contents

1	Introduction	1
1.1	White Dwarfs	1
1.2	G 29-38 Background	2
1.3	Dust Cloud	2
1.4	Possible Companion	3
2	Methods	3
2.1	Fourier Transforms	3
2.2	Pyriod and Lightkurve	5
2.3	Lightcurve Modeling and Fitting	5
3	Analysis and Preliminary Results	6
3.1	Historical Lightcurves	6
3.2	TESS Lightcurves	8
3.3	Pulsation Mode Comparisons	10
3.4	Mode Identifications	12
3.5	Folded Lightcurve Fits	14
3.6	Full Lightcurve Fits	15
4	Future Study	16
4.1	HST Time Series Data	16
4.2	Surface Modeling	18
5	Conclusion	20
	References	21
	Appendices	24
A	TESS FTs	24
B	Folded Lightcurve Fits	27
B.1	Firsthalf fit: 499.676444 $\ell = 2$: $m = 0$	27
B.2	Firsthalf fit: 499.676444 $\ell = 2$: $m = 1$	28
B.3	Firsthalf fit: 499.676444 $\ell = 2$: $m = 2$	29
B.4	Firsthalf fit: 499.676444 $\ell = 2$: $m = -1$	30
B.5	Firsthalf fit: 499.676444 $\ell = 2$: $m = -2$	31

B.6	Firsthalf fit: 499.676444 $\ell = 1$: $m = 0$	32
B.7	Firsthalf fit: 499.676444 $\ell = 1$: $m = 1$	33
B.8	Firsthalf fit: 499.676444 $\ell = 1$: $m = -1$	34
B.9	Secondhalf fit: 499.735414 $\ell = 1$: $m = 0$	35
B.10	Secondhalf fit: 499.735414 $\ell = 1$: $m = 1$	36
B.11	Secondhalf fit: 499.735414 $\ell = 1$: $m = -1$	37
B.12	Secondhalf fit: 499.735414 $\ell = 2$: $m = 0$	38
B.13	Secondhalf fit: 499.735414 $\ell = 2$: $m = 1$	39
B.14	Secondhalf fit: 499.735414 $\ell = 2$: $m = 2$	40
B.15	Secondhalf fit: 499.735414 $\ell = 2$: $m = -1$	41
B.16	Secondhalf fit: 499.735414 $\ell = 2$: $m = -2$	42
B.17	Secondhalf fit: 769.861399 $\ell = 1$: $m = 1$	43
B.18	Secondhalf fit: 769.861399 $\ell = 1$: $m = 0$	44
B.19	Secondhalf fit: 769.861399 $\ell = 1$: $m = -1$	45
B.20	Secondhalf fit: 769.861399 $\ell = 2$: $m = 0$	46
B.21	Secondhalf fit: 769.861399 $\ell = 2$: $m = 1$	47
B.22	Secondhalf fit: 769.861399 $\ell = 2$: $m = 2$	48
B.23	Secondhalf fit: 769.861399 $\ell = 2$: $m = -1$	49
B.24	Secondhalf fit: 769.861399 $\ell = 2$: $m = -2$	50
C	Firsthalf Lightcurve Fit	51
D	Secondhalf Lightcurve Fit	53

1 Introduction

1.1 White Dwarfs

White Dwarf stars represent the last phase in life of most main sequence stars, our Sun included. As a star slowly runs out of fuel to ‘burn’ in its core, it expands and sheds its outer layers (in a red giant phase) and what is left collapses under its own gravity. The remaining gas becomes denser and denser until the only force abating gravity is the electron pressure of the atoms in the star. This pressure is known as ‘electron degeneracy’, and the star must be incredibly dense at this point to encounter such a phenomenon. White Dwarfs have been observed to have masses between $0.1 - 1.3 M_{\odot}$, with the large majority falling between $0.5 - 0.7 M_{\odot}$ [6]. At $1.4 M_{\odot}$ and above, the gravitational pressure exceeds that of the electron degeneracy, and the star will go supernova. This mass is known as the Chandrasekhar limit (after scientist Subrahmanyan Chandrasekhar). In this $0.5 - 0.7 M_{\odot}$ mass range, WDs typically have radii of only 0.8–2.0% of the Sun (comparable to that of the Earth), giving them densities of nearly 10^6 g/cm^3 , or 10,000 times the density of our Sun’s core [7]. Upon formation, WDs are extremely hot from the leftover energy of the star’s earlier stages and the immense increase in density of its core. Afterwards, however, the WD has very little source of fusion energy, and slowly cools by radiating out its energy over billions of years.

Table 1: WD Classifications

Classification	Composition	Suffix	Meaning
DA	H only	P	Magnetic with polarization
DB	He I, no H or metals	H	Magnetic without polarization
DC	Continuous spectrum	E	Emission lines
DO	He II with He I or H	V	Variable
DZ	Metal lines present	X	Peculiar
DQ	Carbon present	d	Circumstellar dust

Note: Suffixes can apply to different classifications, and one star may have multiple suffixes. Adapted from Kaler (2011) [6].

White Dwarf stars have different properties depending on how they were formed. Building off of the standard stellar spectral categories of OBAFGKMLT, we categorize WDs similarly. WDs that carry strong hydrogen lines (indicating the presence of a hydrogen rich atmosphere), like their main sequence cousins, are given the designation ‘A’, or ‘DA’ where the ‘D’ stands for dwarf. Helium dominated atmospheres are given ‘DB’, again like their main sequence cousins. White Dwarf stars usually consist of 3 primary layers: a core of degenerate matter (mostly carbon and oxygen, which crystallizes in lower temperature WDs), a convection zone, and a layer of gas at the surface (the atmosphere). Unlike main sequence stars, WDs typically contain very pure atmospheres of either hydrogen or helium, with very little mixing. This atmospheric purity is

thought to arise from the extreme surface gravity present in WDs, effectively sorting the atmosphere by mass [6]. These atmospheres are also very thin (on the order of hundreds of meters) and comprise only a tiny fraction of the star’s total mass. Other classifications for WDs based on the composition of their atmospheres are shown in Table 1.

As with main sequence stars, WDs are subject to the ‘instability strip’ in the Hertzsprung-Russel (HR) diagram, between temperatures of 10,500 and 13,000 Kelvin [6]. Here we find the DAV WDs (also known as ZZ Ceti stars, after the first one discovered), which vary non-radially over multiple periods with small amplitudes. These are g -mode pulsations, caused by the ionization layers of hydrogen in the star’s atmosphere pulsing against the force of gravity, similar to the wobbling of a water balloon. At around 20,000 Kelvin, the DBV dwarfs undergo a similar process, this time with the ionization of the helium layer in the star’s atmosphere.

1.2 G 29-38 Background

Giclas 29-38 (also known as ZZ Piscium, WD 2326+049, EG 159, and LTT 16907) is a variable WD of type DAV, first cataloged as a variable by Shulov & Kopatskaya in 1974 [8]. G 29-38 is an especially important DAV in the context of its location (57 light years away [9]) and brightness (13.0 apparent magnitude [10], bright enough for the pulsations of the star to be observed by smaller telescopes like TESS) relative to other DAVs, and has been determined to have a mass of $0.71 M_{\odot}$, a radius of $0.01 R_{\odot}$, a surface gravity of $8.02 \pm 0.03 \times \log(g)$, and a temperature of $11,296 \pm 198$ Kelvin [11]. Like other DAVs, G 29-38 exhibits g -mode pulsations, with many individual periods ranging from around 100–3,000 seconds, with most pulsation modes having periods between 300–800 seconds (see Tables 8, 9, 10 in Appendix A). Unlike other DAVs, however, G 29-38 has been found to be ‘contaminated’ with heavy elements that are detectable in its atmosphere. This means that it is also often classified as DAZ, ignoring the variable designation ‘V’. While G 29-38 has been a subject in many studies about WDs and DAVs, Scot J. Kleinman was one of the first to perform in-depth analysis of the star’s pulsation modes in his Ph.D. thesis [1] and subsequent paper [2].

1.3 Dust Cloud

In 1987, B. Zuckerman & E.E. Becklin detected excess infrared radiation around G 29-38 between wavelengths of 2 and $5 \mu\text{m}$ [12]. This radiation was not expected from extrapolations of previous near-infrared spectra of G 29-38, and was inferred to have a temperature of $1,200 \pm 200$ Kelvin [12]. While some theorized that this excess radiation could have been due to a brown dwarf companion star (see Section 1.4), others believed this to be a circumstellar disk, possibly consisting of interstellar dust or debris from a disrupted comet or asteroid. Using observations from the Spitzer Space Telescope, Reach et al. [13] compared the infrared spectrum of G 29-38’s disk to that of the interstellar medium, comet Hale-Bopp, and the Zodiacal light. Reach et al. reached the conclusion that the disk consists of small grains of carbon and silicate dust, between $1\text{--}10 R_{\odot}$ from the star (close for a WD). They estimated that the total mass of the dust to create an infrared signal

similar to that detected must be around 10^8 g, with the possibility of more mass not being detected (likely because it is too cool). Due to the composition of the dust and the fact that similar features are not seen in other DAVs like G 29-38, the authors postulate that this disk could have been caused by the disruption of a comet that passed close to the star, but other possibilities do exist.

Earlier, in Section 1.2, we discussed the fact that G 29-38 has heavy metals detectable in its atmosphere. Since WDs have such high surface gravity, any heavy elements in the atmosphere should sink, meaning that if they are detected they must be being actively replenished. We believe that this dusty disk detected around G 29-38 is actively being accreted onto the star, populating the atmosphere with heavy elements. To prove this, we build off work by Montgomery et al. (2008) [14], which provides methods for modeling the accretion of metals onto a WD, and Thompson et al. (2010) [15], which attempted to map the distribution of calcium across G 29-38 (finding accretion at the poles). The modeling of G 29-38’s surface is further discussed in Section 4.2.

1.4 Possible Companion

When the excess infrared radiation around G 29-38 was first detected, Zuckerman & Becklin immediately suggested the possibility of a companion star [12]. Zuckerman & Becklin theorized that if the radiation was due to a single star, it would have a radius of about $0.15 R_{\odot}$. More recent observations, however, have all but disproved this theory. Specifically, Kuchner et al. (1998) used speckle interferometry at the Keck telescope to obtain extremely high resolution imagery in the K band (infrared). They did not find a point-like source (as one would expect if the stellar companion theory was true), and concluded that if a companion does exist then it must only be separated from G 29-38 by a maximum distance of 0.42 AU [16]. This led Kuchner et al. to propose that the excess radiation does not originate from a companion star but rather a dust cloud, as discussed in Section 1.3.

2 Methods

2.1 Fourier Transforms

The Fourier Transform is one of the most valuable tools that mathematics has given us, with applications everywhere, from sound, electricity, speech recognition, and much more. Essentially, the Fourier Transform (FT) is a way of breaking up a complicated waveform signal into its simple sine wave components. A visual example of the results of this process can be seen in Figures 1 and 2. The signal (Figure 1), which originally appears complicated, is really just the combination of three simple sine waves (shown in Figure 2).

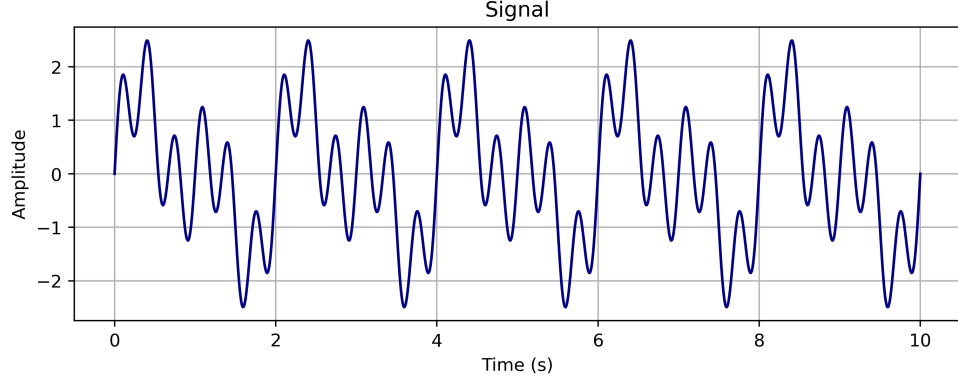


Figure 1: Example Signal

Mathematically, the FT revolves around Equation 1.

$$\hat{f}(\xi) = \int_{-\infty}^{\infty} f(t)e^{-i2\pi\xi t} dt \quad (1)$$

Here, $f(x)$ represents our input signal, ξ represents the frequency of the sine wave, t is the time, and the output, $\hat{f}(\xi)$ is a function of that displays the amplitude of each frequency (called a periodogram). In practice, we use the discrete FT, shown in Equation 2. We can see an example of the output of a discrete FT in Figure 6a. The amplitude is simply how prevalent each frequency is in the signal.

$$\hat{f}(\xi) = \sum_{n=1}^{N-1} f(n)e^{-2\pi i\xi n/N} \quad (2)$$

This simple process forms the basis for most of our understanding of pulsation modes. We can now take a complicated input signal (say, the pulsations of a DAV) and break it apart into its individual pulsation components, called modes.

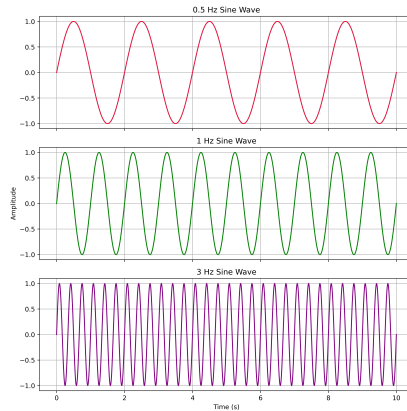


Figure 2: Individual sine wave components of the signal in Figure 1

2.2 Pyriod and Lightkurve

Pyriod is a python library specifically designed by Keaton Bell to perform FTs on lightcurve data [17]. It allows for the direct implementation of TESS lightcurves into Pyriod. The program then outputs a periodogram, which the user can click on to identify specific peaks. Pyriod then subtracts the peak and adds it to a result table, like the one seen in Table 8. Pyriod was used in conjunction with Lightkurve [18], which is a library that allows for easy access to TESS data products through python.

Another method used for creating periodograms is AstroPy’s Lomb-Scargle periodogram function [19].

2.3 Lightcurve Modeling and Fitting

This study used the white dwarf modeling code, ‘pulse_fit2.py’, to computationally create lightcurves using the physics of WDs (from Montgomery (2005) [3] and Montgomery et al. (2010) [4]), which are then fit to the actual lightcurves captured by TESS. As specified in Montgomery (2005), this modeling technique makes several assumptions:

1. The flux perturbations beneath the convection zone of the star are sinusoidal in time and have the angular dependence of a spherical harmonic.
2. We treat the pulsations (on a local scale) as though they are radial.
3. The convective turnover timescale is short enough to be ignored (which is given weight by the fact that the pulsation periods of G 29-38 are hundreds of times longer than the standard convection models of WDs predict the convective turnover time to be [3]).
4. Large scale fluid dynamics within the convective zone are ignored, and we only consider flux and temperature variations.

We then relate the flux entering the base of the convection zone (F_{base}) to the flux leaving the photosphere (F_{phot}) of the star by Equation 3:

$$F_{\text{phot}} = F_{\text{base}} + \tau_C \frac{dF_{\text{phot}}}{dt}, \quad (3)$$

Where $\tau_C \equiv \tau_C(F_{\text{phot}})$ describes the changing heat capacity of the convection zone as a function of F_{phot} . τ_C is then parameterized by Equation 4:

$$\tau_C = \tau_0 \left(\frac{T_{\text{eff}}}{T_{\text{eff},0}} \right)^{-N}. \quad (4)$$

Here τ_0 is the equilibrium value of τ_C , T_{eff} is the instantaneous effective temperature, and $T_{\text{eff},0}$ is its equilibrium value. N is a parameter describing the sensitivity of the changing heat capacity to changes in T_{eff} , which we expect to be around 90 in DAVs [4]. Coupling this with our first assumption, we can then

calculate the flux at the base of the convection zone in the star using Equation 5:

$$\frac{\delta F_{\text{base}}}{F_{\text{base}}} = \text{Re} \left\{ \sum_{j=1}^M A_j e^{i(\omega_j t + \phi_j)} Y_{\ell_j m_j}(\theta, \phi) \right\} \quad (5)$$

Here, A_j , ω_j , ϕ_j , ℓ_j , and m_j are the amplitude, frequency, phase, ℓ , and m values of the j th mode, respectively, with total number of modes equalling M . The code has been adapted to fit to a given lightcurve, taking inputs of the frequency, ℓ , and m value of each given mode and fitting the amplitude, and phase of each mode, as well as the τ_C , N , and inclination angle of the star. This fitting is done using SciPython’s minimize routine, fitting all variables in parallel to increase efficiency [20]. Fitting outputs can be seen in Appendix B and C.

3 Analysis and Preliminary Results

In this section we present our analysis of TESS lightcurves from 2021 and 2022, comparisons of how G 29-38 appeared in the past to the present, current mode identifications by Uzundag et al. [5], and our own estimates of certain mode identifications.

3.1 Historical Lightcurves

As a baseline for how G 29-38 has evolved over time, and to check the consistency of pulsation modes, we compare the newly captured TESS data with historical lightcurves. The historical lightcurves presented here were captured between 1985 and 1993 by the Whole Earth Telescope (WET) and the McDonald Observatory. These observations were presented by Scot J. Kleinman [1].

Table 2: Historical G 29-38 Observations

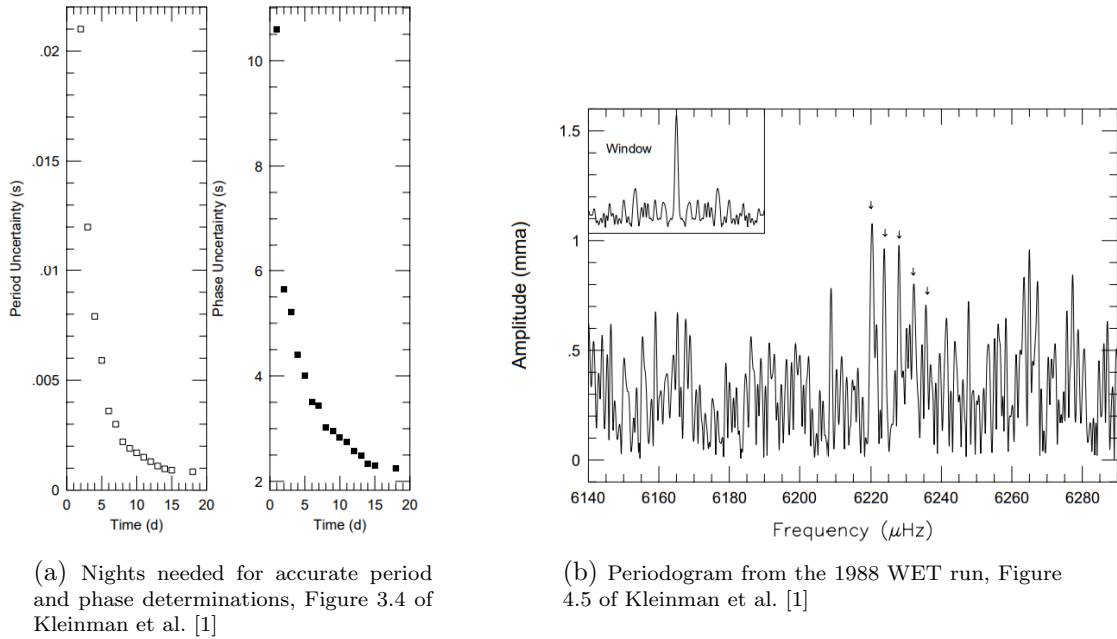
Observation Location(s)	Collection Date	Time on Target
McDonald & SAAO	August / September ’85	23 nights
WET	November / December ’88	40 nights
McDonald	August / September ’89	20 nights
WET	September ’92	11 nights
McDonald	September ’93	9 nights

Note: SAAO is the South African Astronomical Observatory. Months are not exact; some observations took place in adjacent months. Adapted from Kleinman [1].

The WET is essentially a network of telescopes and observers around the globe. This allows for more detailed observations of astronomical objects, especially when continuous time series data is needed (as in our case). Having telescopes spread across the world improves this type of data for several reasons. To

start, it avoids every astronomer’s worst nightmare: daytime. The WET allows for at least one, if not two or more, observation location to be observing the night sky at all times, allowing for the continuous monitoring of an object without the intrusion of the sun. It also minimizes the adverse effects of the atmosphere: overlaps in captures allows for the removal of atmospheric defects like air mass, and having multiple locations theoretically keeps one location with a clear sky even when another is experiencing clouds or storms. Further details of how the WET operates and how multiple observation locations improves data collection can be found in Nather et al. (1990) [21].

Figure 3



While the McDonald Observatory is one of the many parts of the WET, Kleinman also used McDonald on its own to supplement the WET observations, acquiring more detailed and longer timescale sections of data on G 29-38. In fact, both in Kleinman’s original observations and the data presented here, McDonald accounts for most of the data acquisition. In order to ensure a high enough quality of observations to take accurate Fourier Transforms (FTs) of the captured lightcurves, immense amounts of data was needed over long timescales. Figure 3a shows the time needed to accurately determine the period and phase of a specific mode in G 29-38 (as observationally determined by Kleinman [1]) approaches nearly two weeks, minimum. Table 2 shows the WET and McDonald observations that we included in our comparison (Section 3.3) with the TESS data. While much more data was acquired, these chunks were identified by Kleinman as the highest quality and had the greatest consistency of observation.

After these lightcurves are captured, the real fun begins. The data must be cleaned and reduced to exclude defects and atmospheric artifacts, and then Fourier Transforms (FTs) can be performed on the

remaining signal, as discussed in Section 2.1. An example of one of the periodograms from Kleinman’s FTs is shown in Figure 3b. From these FTs we can then isolate the frequencies and amplitudes of individual pulsation modes. Obviously, the signal-to-noise of the data is of utmost importance: while large amplitude modes are easily identifiable, smaller amplitude modes are likewise easily lost among noise. These smaller amplitude modes are just as important to understanding the star, especially because we expect some modes to vary in amplitude over time. The modes identified from this historical data that were used here were mostly of high confidence. We will touch more on the confidence of these modes in a later section.

3.2 TESS Lightcurves

Table 3: TESS G 29-38 Observations

Sector	Start Date	End Date	Year
Sector 42	August 21	September 13	2021
Sector 56	September 2	September 30	2022

Note: Sector 42 contains an 7.5 day gap in data acquisition (see Figure 5a). This is a real thorn in our side later. Sector 56 only has a .8 day gap (see Figure 5b).

The Transiting Exoplanet Survey Satellite (TESS) performed two data acquisition runs on G 29-38, the details of which are shown in Table 3. TESS has both advantages and disadvantages over the ground based observations. Unlike ground based telescopes, being in space allows for continuous observation of targets. The Earth stays out of the way (for the most part), there are no atmospheric artifacts, and without the atmosphere the light from the sun can be avoided much more easily.

Having been launched into space on a rocket in April of 2018, however, TESS is a much smaller telescope than the ones used on the ground. It has an effective aperture of around 10 cm, whereas the smallest telescope at McDonald used for G 29-38 observations is 36 inches (91.4 cm), not counting some of the observations done with the 82 inch Otto Struve telescope at McDonald or the WET (which effectively increases the aperture when overlapping data). This smaller aperture of TESS affects the signal-to-noise ratio (SNR) of the lightcurves we receive from the satellite. As touched on earlier, we cannot simply increase the collection time (as we would do with other types of astronomical observations to increase SNR) as the pulsations of DAVs occur on short timescales. Every data point in the TESS time

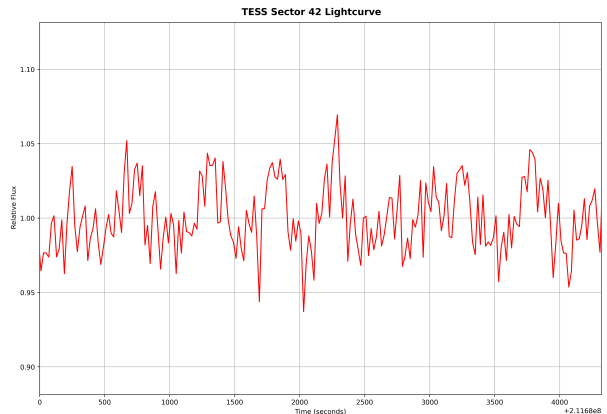
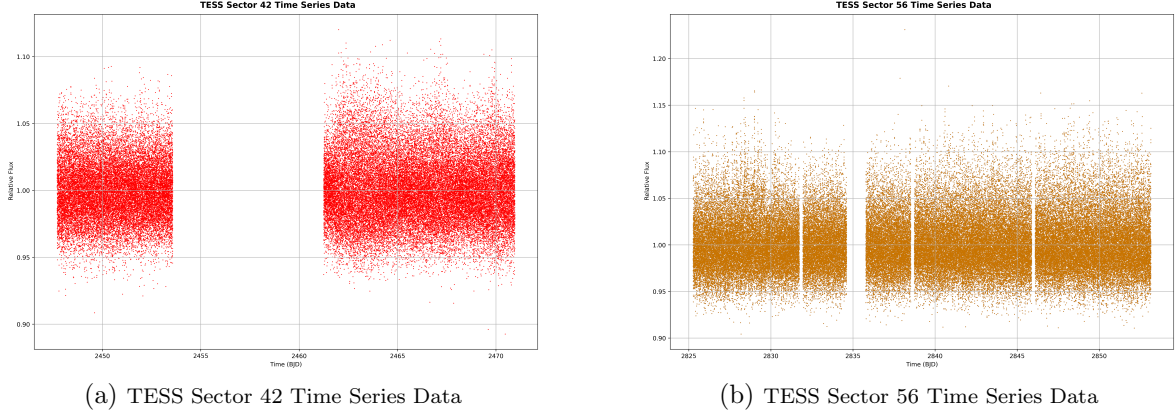


Figure 4: A small chunk of the TESS Sector 42 lightcurve

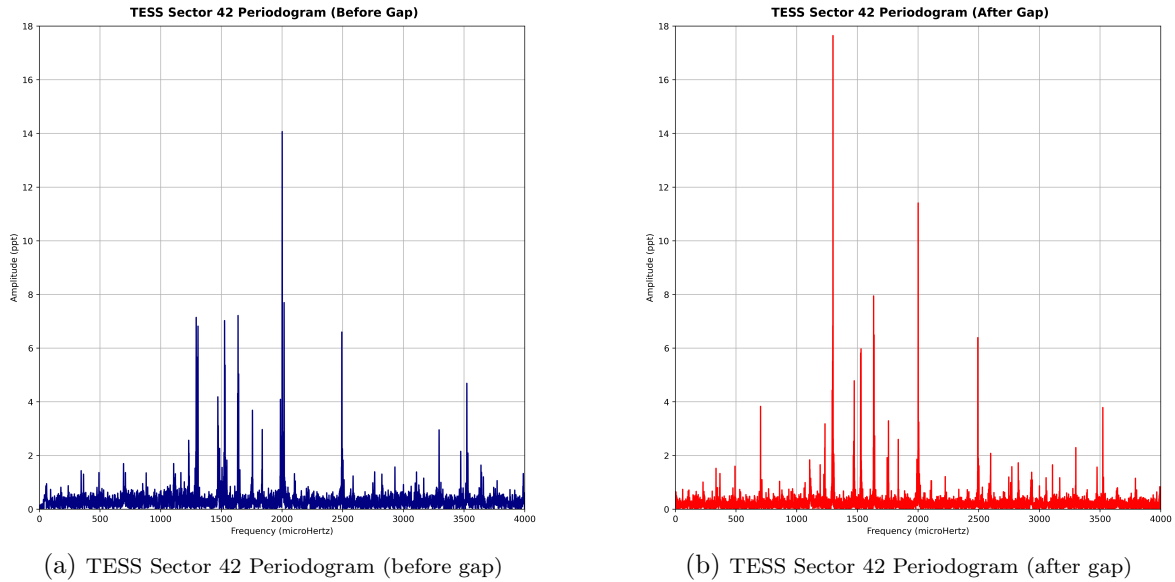
series has a 20 second integration time. A section of TESS lightcurve displaying the random variance due to noise is shown in Figure 4.

Figure 5



Regardless of the noise present in the TESS lightcurves, the sheer amount of continuous data from TESS, without negative impacts from the atmosphere, is extremely valuable. Using Pyriod (as discussed in Section 2.2), we can take FTs of our TESS lightcurves. Because of the large 7.5 day gap in Sector 42, we took two FTs of this Sector, one before and one after the gap. All three periodograms from these FTs are shown in Figures 6a, 6b, and 7. Pyriod then outputs estimates of specific mode frequencies, phases, amplitudes, etc. We can see these results in Tables 8, 9, and 10.

Figure 6



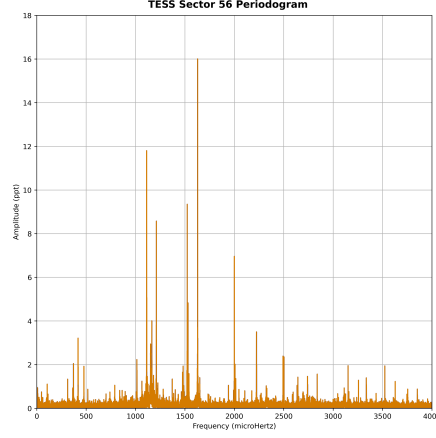


Figure 7: TESS Sector 56 Periodogram

3.3 Pulsation Mode Comparisons

Now that we have FTs with frequencies, phases, and amplitudes of specific pulsation modes from both historical G 29-38 observations and our new TESS observations, we can compare the two datasets to see how much G 29-38 has changed between 1985 and 2022, check the consistency of pulsation modes within the star, and confirm lower SNR modes seen in ground based observations. Even though the TESS data is not perfect and has low SNR on an image to image basis, the sheer volume of data allows for low amplitude modes (1.5-2 ppt) to be detected above the noise. If we can then also observe a mode of the same pulsation frequency in our historical data from McDonald / the WET, then we can safely assume that this is a real mode being produced by the star. Figure 8 shows the full range of pulsation modes detected in the historical data and the TESS data. Figure 9 shows a smaller subset of this data that allows for better observation of mode consistency (or lack thereof) in a range of frequencies that is relevant to our lightcurve fitting (Section 3.5).

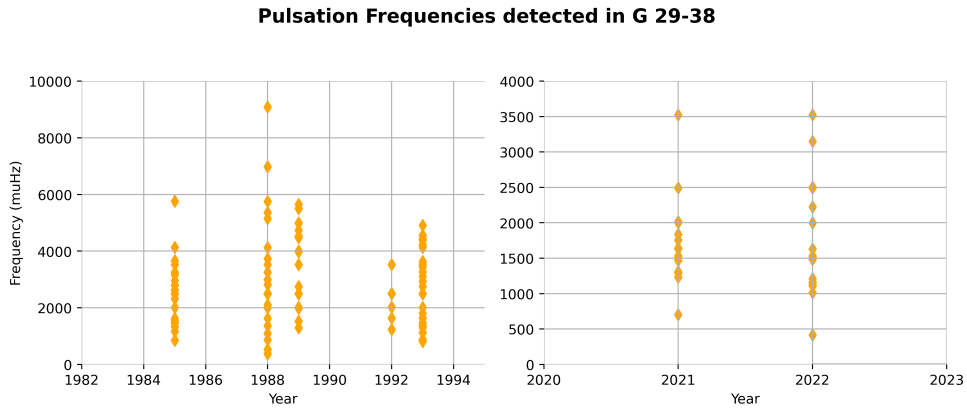


Figure 8: Pulsation Frequencies detected in G 29-38 over 40 years of observations

From this immense amount of data we have a front row seat to an (as of right now) unexplained phenomenon. Even the modes that have consistent frequencies (see the 2492 mode in Figure 9) have extremely variable

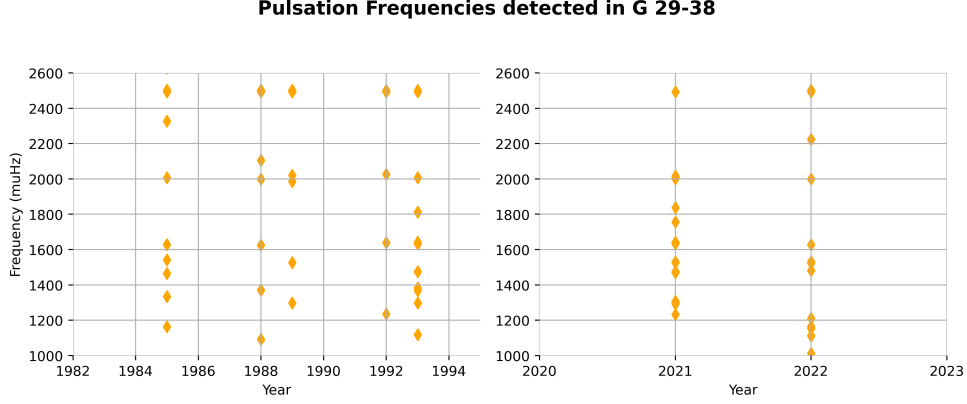


Figure 9: Pulsation Frequencies detected in G 29-38 over 40 years of observations (zoom)

amplitudes. Over the course of years, months, or even days, we have seen amplitudes of pulsation modes in G 29-38 vary greatly or even disappear entirely. Of course, we suspect that these modes did not actually disappear, but rather are so faint that they are not visible in our observations. Figure 10 is an example of these amplitude fluctuations. Both of these modes were chosen because they appear with non-zero amplitudes in all of our chosen datasets. Note that both of these modes are towards the higher end in the pulsation frequencies detected in G 29-38.

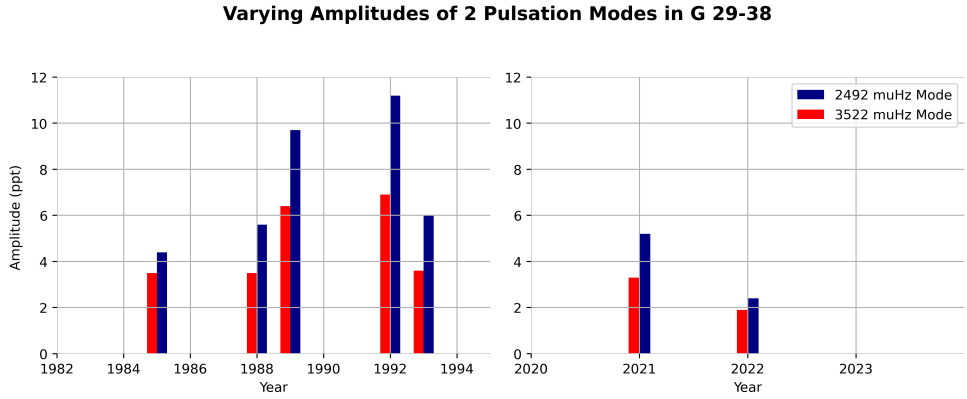


Figure 10: Amplitudes of two selected pulsation modes over 40 years of observations

On an even shorter timescale, we can directly compare the amplitudes of the pulsation modes detected in the two halves of the Sector 42 run. An overlay of the two periodograms from Sector 42, showing the variability in amplitudes of G 29-38's pulsation modes (specifically the 1298 μHz mode), can be seen in Figure 11. This extreme volatility provides us with an additional challenge when we get to modeling G 29-38's lightcurve later (Section 4.1).

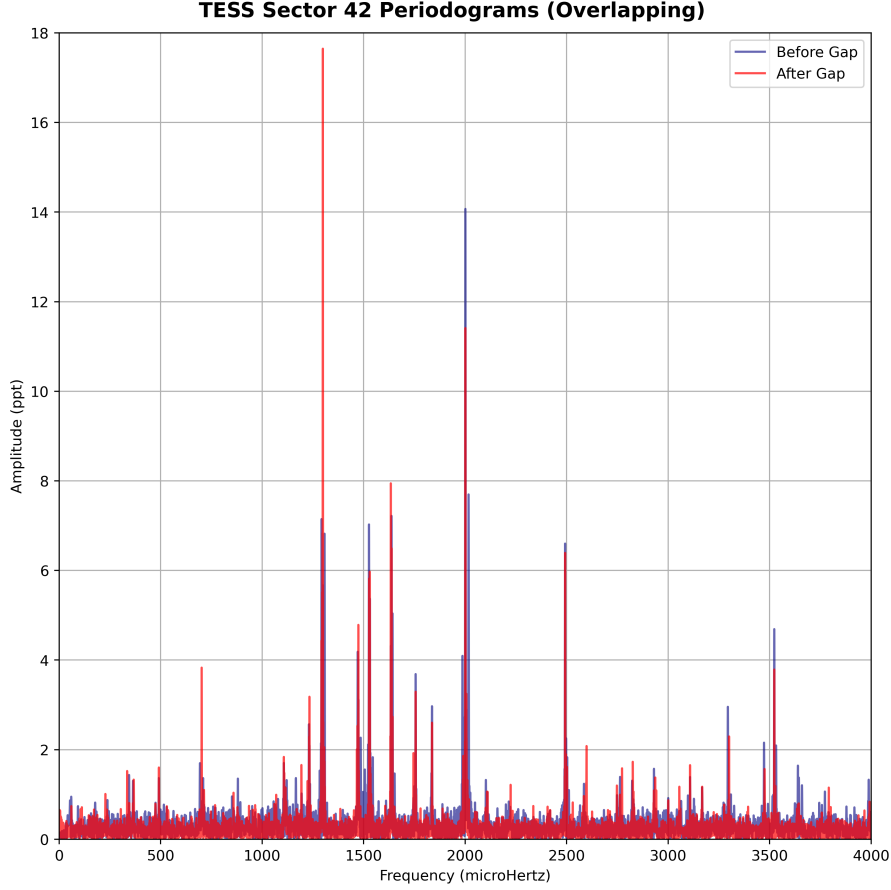


Figure 11: Overlapping periodograms of Sector 42. Blue is before the gap, red is after the gap. Note the drastic amplitude changes in some modes

3.4 Mode Identifications

In order to model the pulsations of G 29-38 using the modeling code, ‘pulse_fit2.py’, (discussed in Section 2.3), we need the periods, ℓ and m values, and initial guesses of the amplitudes and phases of all the modes we wish to fit. For the periods and amplitude estimates, we go to our FTs that were collected in Section 3.2. For ℓ and m mode identifications, we reference Murat Uzundag et al. (in preparation) [5]. This paper details the process of identifying the ℓ and m values of 30 pulsation modes in G 29-38. Using rotational multiplet and asymptotic period spacing techniques (based on previous work by Winget et al. (1994) [22] and others), Uzundag et al. were able to identify 14 $\ell = 1$ modes and 16 $\ell = 2$ modes in the TESS Sector 42 and 56 datasets. Table 3 of Uzundag et al. contains all the detected pulsation modes of both Sector 42 and 56 and their associated ℓ and m values, when applicable. An adaptation of this table is shown here as Table 4.

Table 4: G 29-38 Mode Identifications

Frequency (μHz)	Period (s)	Amplitude (ppt)	S/N	k	ℓ	m
740.059* (21)	1351.244 (13)	0.742 (69)	6.87			
838.89* (18)	1192.051 (12)	0.857 (69)	7.94	32	1	
864.037* (19)	1157.358 (12)	0.801 (69)	7.42	31	1	
1006.627* (19)	993.417 (11)	0.834 (69)	7.73	47	2	+1
1012.964* (07)	987.202 (10)	2.268 (69)	21.02	47	2	0
1064.336* (13)	939.553 (11)	1.216 (69)	11.27	26	1	
1106.833 (17)	903.478 (14)	1.458 (10)	11.67	25	1	+1
1111.944* (05)	899.326 (10)	11.84 (47)	109.83	25	1	0
1115.196 (33)	896.712 (27)	0.900 (13)	7.50	25	1	-1
1151.511* (06)	868.424 (10)	2.801 (69)	25.96	41	2	-2
1164.353* (04)	858.846 (10)	4.056 (69)	37.59	41	2	0
1181.656* (10)	846.270 (10)	1.49 (69)	13.81	24	1	
1210.47* (02)	826.125 (10)	8.668 (69)	80.35	39	2	+2
1225.755* (30)	815.824 (12)	1.085 (10)	10.06	39	2	0
1232.854 (11)	811.125 (77)	2.197 (10)	17.58	39	2	-1
1279.511* (17)	781.549 (11)	0.914 (69)	8.47	37	2	+2
1292.603 (41)	773.646 (79)	4.240 (13)	35.33	37	2	0
1298.883 (02)	769.892 (14)	10.544 (10)	84.35	37	2	-1
1307.303 (15)	764.942 (66)	2.627 (13)	21.9	37	2	-2
1371.426* (12)	729.168 (10)	1.315 (69)	12.19	35	2	
1401.587* (18)	713.477 (10)	0.85 (69)	7.88	21	1	
1431.995* (25)	698.327 (11)	0.612 (69)	5.67	34	2	
1474.048 (07)	678.403 (35)	3.307 (10)	26.46			
1475.167* (10)	677.889 (10)	1.627 (69)	15.08	33	2	+1
1481.34* (08)	675.065 (10)	1.906 (69)	17.66	33	2	0
1487.704* (14)	672.177 (10)	1.074 (69)	9.96	33	2	-1
1522.859* (02)	656.660 (10)	9.462 (69)	87.7	19	1	+1
1526.590 (05)	655.054 (22)	4.983 (10)	39.87	19	1	0
1530.651* (03)	653.317 (10)	4.959 (69)	45.96	19	1	-1
1539.918* (11)	649.385 (10)	1.467 (69)	13.6	32	2	
1628.166* (01)	614.188 (10)	16.122 (69)	149.43	30	2	
1633.792 (05)	612.073 (19)	5.018 (10)	40.15	18	1	+1
1637.552 (05)	610.667 (19)	5.035 (10)	40.29	18	1	0
1642.383 (09)	608.871 (36)	2.640 (10)	21.12	18	1	-1
1649.424* (11)	606.272 (10)	1.346 (69)	12.48			
1745.251 (18)	572.983 (62)	1.339 (10)	10.72	17	1	+1
1750.641 (36)	571.219 (11)	0.696 (10)	5.57	17	1	0
1756.076 (09)	569.451 (29)	2.796 (10)	22.37	17	1	-1
1836.735 (11)	544.444 (34)	2.186 (10)	17.49	27	2	
1940.523* (15)	515.325 (10)	1.064 (69)	9.86	26	2	
1986.868 (11)	503.304 (26)	1.261 (13)	10.5	25	2	+2
1992.310 (48)	501.930 (12)	0.687 (69)	6.25	25	2	+1
1999.742* (02)	500.065 (10)	6.948 (69)	64.4	25	2	0
2006.51* (09)	498.378 (10)	1.811 (69)	16.78	25	2	-1
2013.93* (12)	496.542 (10)	1.274 (69)	11.81	25	2	-2
2016.620 (26)	495.879 (63)	2.476 (11)	23.14			-
2045.91* (18)	488.780 (10)	0.853 (69)	7.9	15	1	
2104.979* (27)	475.064 (62)	0.809 (99)	7.51	24	2	
2223.76* (04)	449.689 (10)	3.499 (69)	32.43	14	1	
2327.068* (18)	429.725 (10)	0.881 (69)	8.17	22	2	
2492.399 (04)	401.219 (08)	5.216 (10)	41.73	13	1	+1
2497.176* (17)	400.452 (28)	1.455 (10)	11.65	13	1	0
2502.278* (07)	399.636 (10)	2.345 (69)	21.74	13	1	-1
2594.995* (21)	385.357 (10)	0.741 (69)	6.87	20	2	
2747.582 (29)	363.956 (39)	0.845 (10)	6.76	12	1	
3522.773 (07)	283.867 (06)	3.263 (10)	26.11	10	1	
3639.341 (30)	274.775 (23)	0.822 (10)	6.58	15	2	
3754.433* (17)	266.352 (10)	0.893 (69)	8.27			

Mode IDs for pulsation modes in Sector 42 and 56, adapted from Uzundag et al. [5]. Note that some periods are different than those identified in Appendix A because they are averaged over all 3 datasets.

3.5 Folded Lightcurve Fits

Table 5: Folded Lightcurve Fits of the 499.676444 Mode (Before Gap)

Period	Residuals (Squared)	N	ℓ	m
499.676444	2.007762e-07	33.266 +/- 0.042	2	1
499.676444	2.042538e-07	45.422 +/- 0.008	2	-1
499.676444	2.109004e-07	20.957 +/- 0.013	1	0
499.676444	2.113389e-07	41.882 +/- 0.190	1	1
499.676444	2.131638e-07	41.608 +/- 0.036	1	-1
499.676444	3.106761e-07	15.000 +/- 0.003	2	0
499.676444	3.353059e-07	15.000 +/- 0.007	2	-2
499.676444	3.355401e-07	15.000 +/- 0.024	2	2

Note: Fits with N value approaching 15 are most likely incorrect. This is because N = 15 is the lower limit for N value fitting, and the minimize parallel routine is finding a local minimum at the very edge of the possible parameter space.

Table 6: Folded Lightcurve Fits of the 499.735414 Mode (After Gap)

Period	Residuals (Squared)	N	ℓ	m
499.735414	6.754501e-07	33.642 +/- 0.011	2	1
499.735414	6.919045e-07	15.010 +/- 0.007	2	0
499.735414	6.945130e-07	15.000 +/- 0.286	1	0
499.735414	7.155307e-07	45.870 +/- 0.006	2	-1
499.735414	7.361092e-07	57.303 +/- 0.081	1	1
499.735414	7.365652e-07	55.447 +/- 0.079	1	-1
499.735414	9.095223e-07	15.000 +/- 0.055	2	-2
499.735414	9.096486e-07	15.000 +/- 0.025	2	2

Note: Fits with N value approaching 15 are most likely incorrect. This is because N = 15 is the lower limit for N value fitting, and the minimize parallel routine is finding a local minimum at the very edge of the possible parameter space.

We begin by modeling G 29-38's lightcurve through lightcurve folding. This involves 'folding' the lightcurve on itself at every period of a certain pulsation mode, resulting in a much higher SNR lightcurve containing only the selected mode (technically all the other modes are still there, but they are averaged out since the lightcurve is not folded by their periods). An example of a folded lightcurve is shown in Figure 12. This technique allows for us to test the WD modeling code introduced in Section 2.3 on a single periodicity at a time. This technique was used to independently verify the ℓ and m values for two pulsation modes: the 500 second mode and the 769 mode. These modes were chosen because they have the highest amplitudes in the Sector 42 datasets. The code was run for $\ell = 1$ and $\ell = 2$ and all possible m values, using three folded lightcurves. The first being folded over the 500 second mode in the first half of Sector 42 (before the gap), the second folded over the 500 second mode in the second half of Sector 42 (after the gap), and the third folded over the 769 second mode in the second half of Sector 42 (after the gap). The 769 second mode was

not folded in the first half of Sector 42 because its amplitude is very small (see Table 8). The quality of each fit can then be evaluated using the output parameters of the code. Tables of every fit done on each folded lightcurve, with output parameters from the White Dwarf Modeling Code, are shown in Tables 5, 6, and 7. More detailed results (along with actual images of each fit) are shown in Appendix B. The best fit ℓ and m values for the 499 second mode are $\ell = 2$ and $m = 1$, in agreement with the mode identifications done by Uzundag et al. (see Table 4). There is not a clear best fit for the 769 second mode, with several fits having similar residual values, including the $\ell = 2$, $m = -1$ identification that Uzundag et al. have identified as the best mode ID.

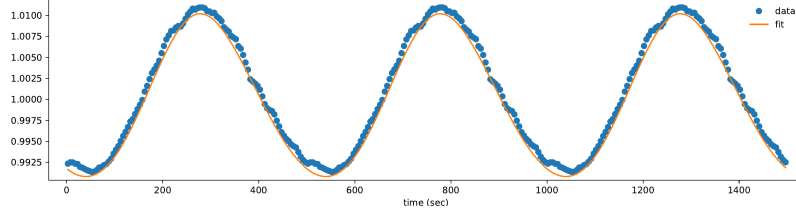


Figure 12: Example of a folded lightcurve.

Table 7: Folded Lightcurve Fits of the 769.861399 Mode (After Gap)

Period	Residuals (Squared)	N	ℓ	m
769.861399	7.643375e-07	17.749 +/- 0.029	2	1
769.861399	7.671935e-07	89.019 +/- 0.024	1	-1
769.861399	7.672443e-07	89.818 +/- 0.228	1	1
769.861399	7.691692e-07	27.003 +/- 0.060	2	-1
769.861399	7.938728e-07	15.451 +/- 0.027	1	0
769.861399	9.811828e-07	15.000 +/- 0.003	2	0
769.861399	2.459392e-06	15.000 +/- 47.478	2	-2
769.861399	2.459396e-06	15.000 +/- 0.084	2	2

Note: Fits with N value approaching 15 are most likely incorrect. This is because $N = 15$ is the lower limit for N value fitting, and the minimize parallel routine is finding a local minimum at the very edge of the possible parameter space.

3.6 Full Lightcurve Fits

We can then begin to fit our entire TESS lightcurves using the WD modeling code discussed in Section 2.3. Using 11 modes with ℓ and m identifications from Uzundag et al., the code was run on the first and second half of the Sector 42 dataset, separately. The resulting output parameters are shown in Tables 11 and 12, respectively. The modeled lightcurves are shown relative to the actual TESS lightcurves in Figures 13 and 14. This shows that we are now effectively modeling the pulsation behavior of the star, only using a few basic input parameters. These fits are not perfect, as discussed in Appendix C and D, and will be improved upon in future work to ensure correct lightcurve fitting.

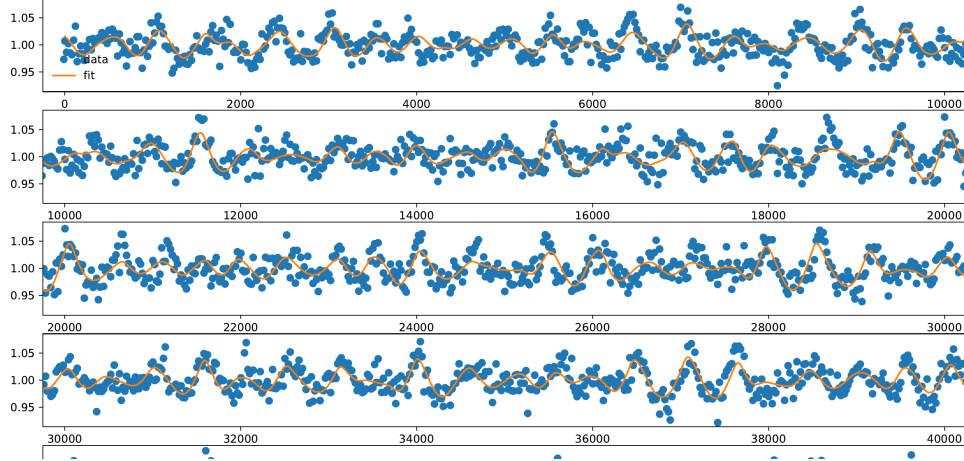


Figure 13: A section of fitted lightcurve from the first half of the Sector 42 dataset. Blue is the TESS lightcurve, orange is the curve generated by the fit. Time (in seconds) is on the x-axis, relative flux is on the y-axis. The entire fit is shown in Figure 17, in Appendix C.

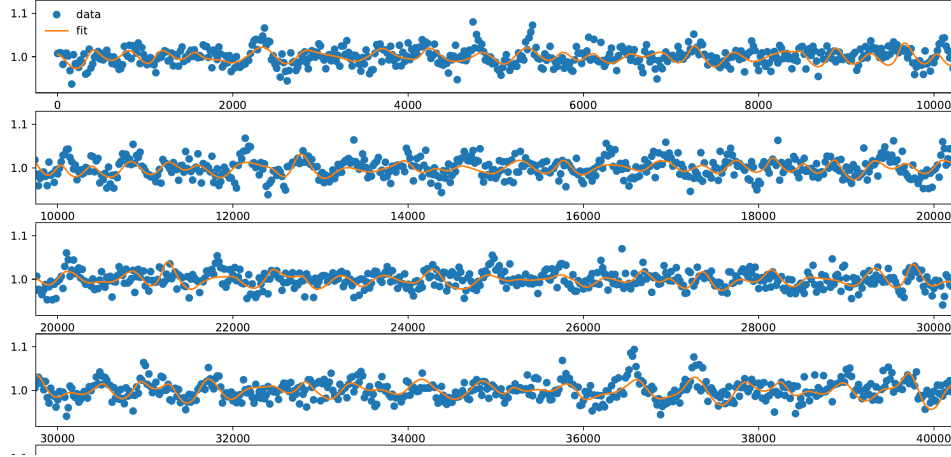


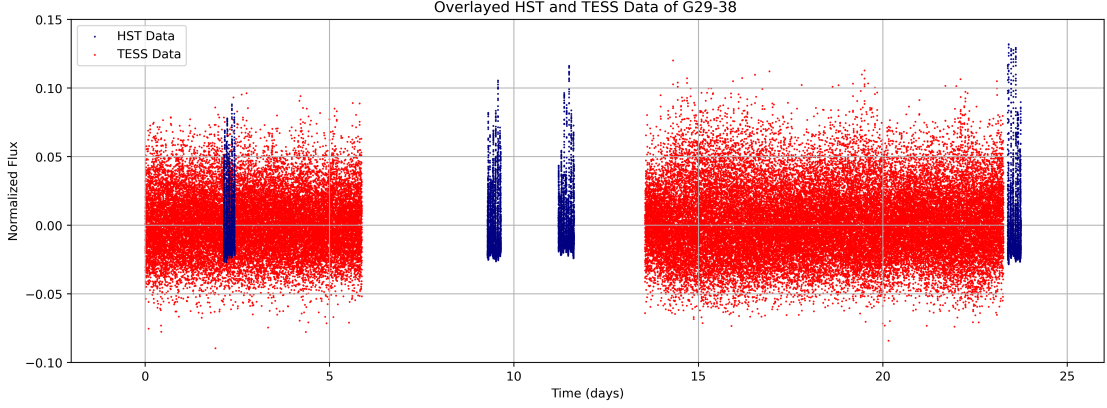
Figure 14: A section of fitted lightcurve from the second half of the Sector 42 dataset. Time (in seconds) is on the x-axis, relative flux is on the y-axis. The entire fit is shown in Figure 18, in Appendix D.

4 Future Study

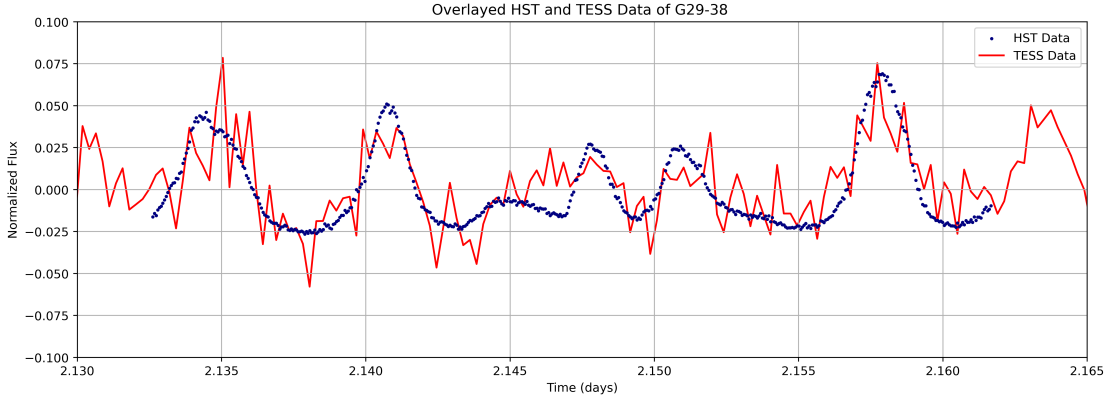
4.1 HST Time Series Data

We have been afforded the luxury of observing time on the legendary Hubble Space Telescope (HST) as part of HST proposal ID 15839 [23], which aims to map the distribution of metals on G 29-38's surface. Over the same time period as TESS's Sector 42 dataset, the HST took 24 sections of time series data (each around 40 minutes). This time series data were acquired with the COS instrument [24], with individual exposures of 4 seconds. The overlap of HST data and TESS Sector 42 data can be seen in Figure 15a. Unfortunately, the gap in the Sector 42 data almost perfectly coincides with over half of the HST data. To make matters worse, a fourth of the HST data was taken just hours after the TESS Sector 42 coverage ended. Because of

Figure 15



(a) HST and TESS Sector 42 Data overlay. HST is blue, TESS is red.



(b) HST and TESS Sector 42 Data overlay (zoom). HST is blue, TESS is red.

the instability of the pulsation mode amplitudes in G 29-38, our modeling of the star's lightcurve in the gap of the TESS data will be an estimate of the stars behavior at best. We hope to have a good estimate of the star's behavior at the end of the Sector 42 dataset, which will allow us to use the HST data there. Where it does overlap, the HST data provides TESS with a huge upgrade in SNR, both because it is a much bigger instrument and because its time series data was taken in the ultraviolet, where G 29-38 radiates more energy, and its relative brightness variations are larger. This increase in data quality can be seen in Figure 15b. The difference in wavelength range is inconsequential for our lightcurve fitting as we are only interested in the changes in relative normalized flux, not the absolute flux detected by the instrument.

The COS instrument also takes integrated spectral products at the same time as it captures the total flux for the time series product. This spectral data will allow us to provide estimates of the chemical composition of G 29-38's atmosphere during individual pulsation events.

4.2 Surface Modeling

Using the pulsation modes identified with TESS, the time series and spectral data from the HST, and our model of G 29-38 that was created using the White Dwarf Modeling Code, we will be able to create an estimate of how the surface of G 29-38 was behaving during our observations. The modeling code, along with mode identifications from Uzundag et al., provide us with a pulsation model of the star’s surface temperature, much like the images shown in Figure 16. Knowing what part of the star’s surface was hot/bright at specific times, along with the composition of the star’s atmosphere at the same time (from HST spectra) will allow us to estimate the star’s atmospheric composition at specific locations. This could provide us with information about G 29-38’s accretion status (i.e. if we see more heavy elements around the star’s equator than at the poles) or evidence for the lack of accretion (i.e. we see a uniform distribution of heavy elements across the star’s surface).

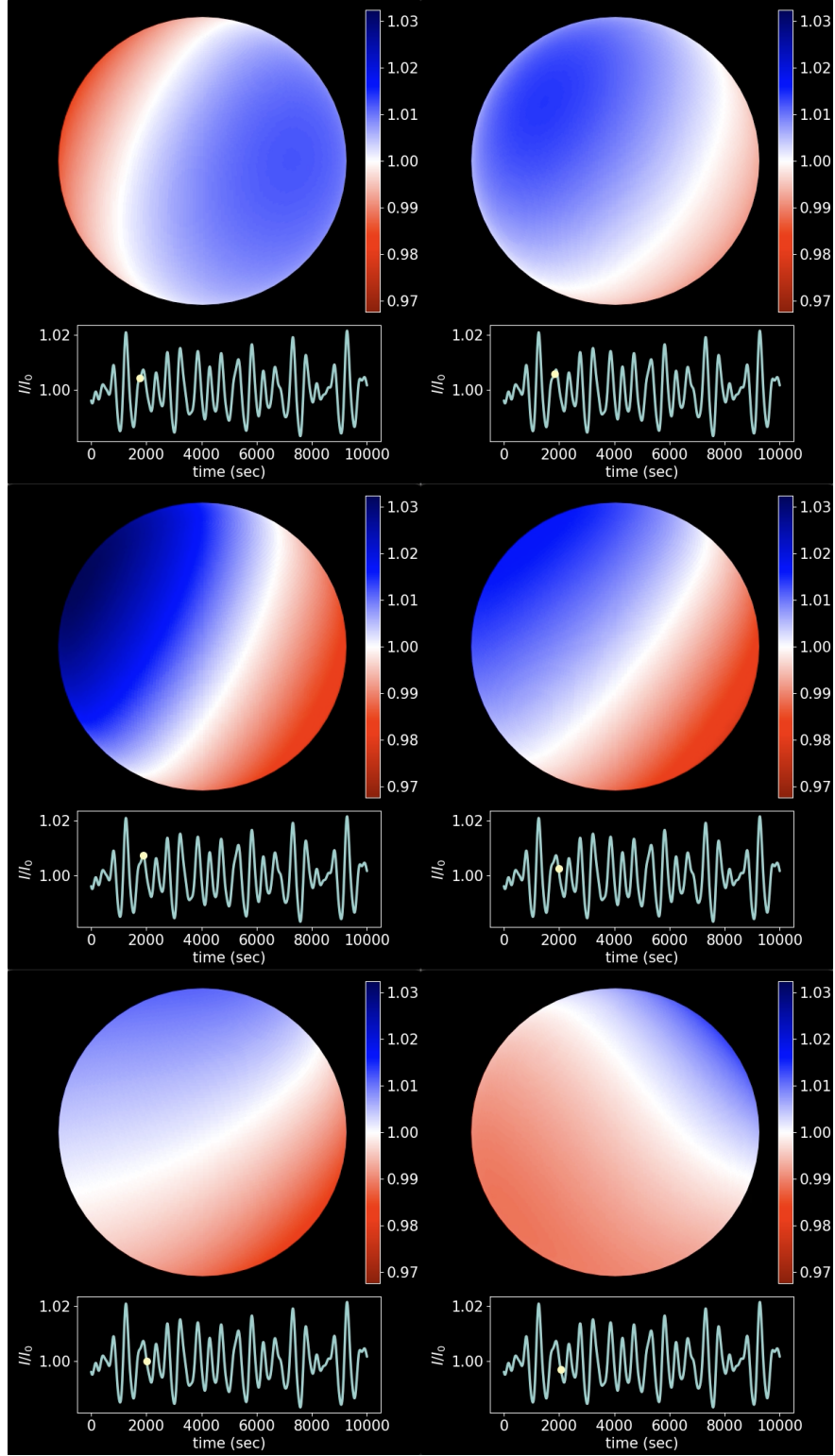


Figure 16: An example of the surface temperature modeling of a WD. Blue is hotter parts of the star, red is cooler; the colorbar shows the relative flux at different points on the star's surface. The point on the lightcurve below each image shows where the star is in its pulsation stage.

5 Conclusion

In this study, advanced Fourier Transform (FT) techniques were used to find individual pulsation modes of DAV G 29-38. These pulsation modes were compared to past observations and used to model the star with Python code based on previous work by Montgomery (2005) [3] and Montgomery et al. (2010) [4]. This model was then used to estimate mode identifications for two of the most prevalent pulsation modes in the Transiting Exoplanet Survey Satellite (TESS) Sector 42 data, and these mode identifications were compared to independently estimated mode IDs found by Uzundag et al. [5]. In one of the two modes tested, we found an agreement in ℓ and m values determined by Uzundag et al. In the other, the fit residuals were too closely spaced to accurately determine a best fit, but the ℓ and m ID recognized by Uzundag et al. was one of the 3 best fits identified by the modeling code.

Future study with data acquired by the Hubble Space Telescope (HST) will allow us to create a temperature map of G 29-38's surface during pulsation events and potentially estimate the composition of specific regions of the star's surface.

References

- [1] Kleinman, S. J. 1995, Ph.D thesis, University of Texas, Austin
- [2] Kleinman, S. J., Nather, R. E., Winget, D. E., Clemens, J. C., Bradley, P. A., Kanaan, A., . . . Kawaler, S. D. (1998, March). Understanding the cool da white dwarf pulsator, G29-38. *The Astrophysical Journal*, 495(1), 424-434. doi:10.1086/305259
- [3] Montgomery, M. H. (2005). A new technique for probing convection in pulsating white dwarf stars. *The Astrophysical Journal*, 633(2), 1142-1149. doi:10.1086/466511
- [4] Montgomery, M. H., Provencal, J. L., Kanaan, A., Mukadam, A. S., Thompson, S. E., Dalessio, J., . . . Koester, D. (2010). Evidence for temperature change and oblique pulsation from light curve fits of the pulsating white dwarf GD 358. *The Astrophysical Journal*, 716(1), 84-96. doi:10.1088/0004-637x/716/1/84
- [5] Uzundag, M., Gerónimo, F. D., Córscico, A. H., Silvotti, R., Bradley, P. A., . . . Nitta, A. (Forthcoming). Asteroseismological analysis of the polluted white dwarf G29–38 with *TESS*. Publication Forthcoming.
- [6] Kaler, James B. *Stars and Their Spectra: An Introduction to the Spectral Sequence*. Cambridge University Press, 2011.
- [7] Shipman, H. L. (1979). Masses and radii of white-dwarf stars. III - results for 110 hydrogen-rich and 28 helium-rich stars. *The Astrophysical Journal*, 228, 240. <https://doi.org/10.1086/156841>
- [8] Shulov, O. S., Kopatskaya, E. N. (1974, January). Variability of the white dwarf g 29-38. *Astrophysics*, 10(1), 72-74. doi:10.1007/bf01005183
- [9] Gaia Collaboration, Vallenari, A., Brown, A., Prusti, T., . . . Zwitter, T. (2022). Gaia data release 3. summary of the content and survey properties. *Astronomy & Astrophysics*. doi:10.1051/0004-6361/202243940
- [10] Van Altena, W. F., Hoffleit, E. D., Lee, J. T. (1995). *General Catalogue of Trigonometric Stellar Parallaxes*. New Haven, CT: Yale Univ. Obs.
- [11] McCleery, J., Tremblay, P.-E., Gentile Fusillo, N. P., Hollands, M. A., Gänsicke, B. T., Izquierdo, P., Toonen, S., Cunningham, T., & Rebassa-Mansergas, A. (2020). Gaia White Dwarfs within 40PC II: The Volume-Limited Northern Hemisphere Sample. *Monthly Notices of the Royal Astronomical Society*, 499(2), 1890-1908. doi:10.1093/mnras/staa2030
- [12] Zuckerman, B., & Becklin, E. E. (1987). Excess infrared radiation from a white dwarf-an orbiting brown dwarf? *Nature*, 330(6144), 138-140. doi:10.1038/330138a0

- [13] Reach, W. T., Kuchner, M. J., Von Hippel, T., Burrows, A., Mullally, F., Kilic, M., & Winget, D. E. (2005). The dust cloud around the white dwarf G29-38. *The Astrophysical Journal*, 635(2). doi:10.1086/499561
- [14] Montgomery, M. H., Thompson, S. E., & von Hippel, T. (2008). Constraining the surface inhomogeneity and settling times of metals on accreting white dwarfs. *The Astrophysical Journal*, 685(2). <https://doi.org/10.1086/592731>
- [15] Thompson, S. E., Montgomery, M. H., von Hippel, T., Nitta, A., Dalessio, J., Provencal, J., Strickland, W., Holtzman, J. A., Mukadam, A., Sullivan, D., Nagel, T., Koziel-Wierzbowska, D., Kundera, T., Zola, S., Winiarski, M., Drozd, M., Kuligowska, E., Ogloza, W., Bognár, Z., . . . Mullally, F. (2010). Pulsational mapping of calcium across the surface of a white dwarf. *The Astrophysical Journal*, 714(1), 296–308. <https://doi.org/10.1088/0004-637x/714/1/296>
- [16] Kuchner, M. J., Koresko, C. D., & Brown, M. E. (1998). Keck speckle imaging of the white dwarf G29-38: No brown dwarf companion detected. *The Astrophysical Journal*, 508(1). doi:10.1086/311725
- [17] Bell, Keaton. (2022). Pyriod: Period detection and fitting routines. Retrieved April 14, 2023, from <https://ui.adsabs.harvard.edu/abs/2022ascl.soft07007B/abstract>
- [18] Lightkurve Collaboration, Cardoso, J., Hedges, C., Gully-Santiago, M., Saunders, N., Cody, A., . . . Barentsen, G. (2018). Lightkurve: Kepler and Tess Time Series Analysis in python. Retrieved April 14, 2023, from <https://ui.adsabs.harvard.edu/abs/2018ascl.soft12013L/abstract>
- [19] Price-Whelan, A. M., SipHocz, BM, G”unther, HM, Lim, P., Crawford, S., Conseil, S., . . . others. (2018). The Astropy Project: Building an open-science project and status of the v2. 0 core package. *The Astronomical Journal*, 156(3), 123.
- [20] Pauli Virtanen, Ralf Gommers, Travis E. Oliphant, Matt Haberland, Tyler Reddy, David Cournapeau, Evgeni Burovski, Pearu Peterson, Warren Weckesser, Jonathan Bright, Stéfan J. van der Walt, Matthew Brett, Joshua Wilson, K. Jarrod Millman, Nikolay Mayorov, Andrew R. J. Nelson, Eric Jones, Robert Kern, Eric Larson, CJ Carey, İlhan Polat, Yu Feng, Eric W. Moore, Jake VanderPlas, Denis Laxalde, Josef Perktold, Robert Cimrman, Ian Henriksen, E.A. Quintero, Charles R Harris, Anne M. Archibald, Antônio H. Ribeiro, Fabian Pedregosa, Paul van Mulbregt, and SciPy 1.0 Contributors. (2020) SciPy 1.0: Fundamental Algorithms for Scientific Computing in Python. *Nature Methods*, 17(3), 261-272.
- [21] Nather, R. E., Winget, D. E., Clemens, J. C., Hansen, C. J., & Hine, B. P. (1990). The Whole Earth Telescope - A New Astronomical Instrument. *The Astrophysical Journal*, 361, 309. doi:10.1086/169196
- [22] Winget, D. E., Nather, R. E., Clemens, J. C., Provencal, J. L., Kleinman, S. J., Bradley, P. A., . . . Grauer, A. D. (1994). Whole Earth Telescope Observations of the DBV White Dwarf GD 358. *The Astrophysical Journal*, 430, 839. doi:10.1086/174455

- [23] Toloza Castillo, O.F.(2019). Mapping the Distribution of Planetary Debris accreted across the surface of White Dwarf G29-38. ID 15839.
- [24] Hubble Space Telescope User Documentation: 5.4 Working with TIME-TAG Data. Retrieved April 14, 2023, from <https://hst-docs.stsci.edu/cosdhub/chapter-5-cos-data-analysis/5-4-working-with-time-tag-data>

Appendix

A TESS FTs

Table 8: TESS Sector 42 Pulsation Modes (Before Gap)

Frequency (μHz)	Frequency Error	Period (seconds)	Period Error	Amplitude (ppt)	Amplitude Error	Phase (radian)	Phase Error
1230.720087	0.083027	812.532444	0.054815	1.833696	0.139507	0.495234	0.012109
1292.725217	0.031122	773.559599	0.018623	5.372751	0.142087	0.277037	0.004208
1297.988882	0.064473	770.422624	0.038268	4.314984	0.177577	0.397854	0.009829
1299.364243	0.143144	769.607141	0.084784	1.908075	0.174733	0.442207	0.022581
1307.428246	0.033614	764.860330	0.019664	4.656699	0.141656	0.679489	0.004837
1470.855952	0.048451	679.876230	0.022396	3.141393	0.139507	0.062607	0.007069
1526.538580	0.029871	655.076795	0.012818	5.325365	0.145232	0.756849	0.004204
1530.217539	0.038857	653.501855	0.016594	4.093233	0.145373	0.739382	0.005469
1633.998056	0.063954	611.995832	0.023953	2.552586	0.145542	0.422545	0.008830
1637.534953	0.037260	610.673988	0.013895	4.626042	0.146301	0.104727	0.004899
1642.312239	0.050678	608.897612	0.018789	3.266007	0.141181	0.662748	0.006877
1756.133585	0.055385	569.432763	0.017959	2.747596	0.139503	0.271443	0.008082
1836.661391	0.068041	544.466174	0.020170	2.237055	0.139486	0.256943	0.009927
1987.032696	0.052607	503.262982	0.013324	2.899606	0.139594	0.966588	0.007674
2001.295062	0.014470	499.676444	0.003613	10.568827	0.139807	0.430333	0.002106
2016.727777	0.026054	495.852743	0.006406	5.861873	0.139760	0.861359	0.003792
2492.361510	0.031070	401.225904	0.005002	4.896581	0.139512	0.597020	0.004535
3294.136254	0.071984	303.569714	0.006634	2.113647	0.139538	0.057986	0.010510
3522.764300	0.043837	283.867984	0.003532	3.470631	0.139548	0.101402	0.006401

Note: Periods and Period Errors are not outputted by Pyriad, but are extrapolated from Frequencies and Frequency Errors

Table 9: TESS Sector 42 Pulsation Modes (After Gap)

Frequency (μHz)	Frequency Error	Period (seconds)	Period Error	Amplitude (ppt)	Amplitude Error	Phase (radian)	Phase Error
702.043386	0.022808	1424.413390	0.046276	3.257602	0.111324	0.866136	0.005445
1106.887265	0.048146	903.434371	0.039296	1.543359	0.111327	0.089769	0.011494
1232.904498	0.026515	811.092831	0.017444	2.803030	0.111350	0.238048	0.006329
1292.467937	0.019492	773.713584	0.011669	4.225660	0.113580	0.921678	0.004276
1295.384872	0.029466	771.971343	0.017560	4.014544	0.125021	0.545318	0.006682
1296.398333	0.028775	771.367854	0.017122	4.079100	0.124080	0.896296	0.006800
1298.965550	0.005384	769.843357	0.003191	15.348717	0.115297	0.556758	0.001207
1469.641820	0.035684	680.437904	0.016522	2.085841	0.111697	0.882891	0.008536
1473.899703	0.018348	678.472217	0.008446	4.056315	0.111693	0.389075	0.004389
1526.705983	0.015395	655.004966	0.006605	4.904862	0.111681	0.141230	0.003657
1530.311158	0.015149	653.461876	0.006469	4.984357	0.111737	0.824522	0.003598
1633.771464	0.011788	612.080711	0.004416	6.463464	0.112460	0.427518	0.002754
1637.582845	0.015161	610.656128	0.005654	5.049450	0.113215	0.918074	0.003523
1642.353038	0.034114	608.882486	0.012648	2.203058	0.112329	0.066846	0.008062
1756.123782	0.026688	569.435942	0.008654	2.784822	0.111334	0.278187	0.006371
1836.684829	0.034838	544.459226	0.010327	2.133222	0.111337	0.369269	0.008317
2001.048753	0.007780	499.737949	0.001943	9.739675	0.111697	0.590782	0.001824
2006.226886	0.028319	498.448110	0.007036	2.676097	0.111690	0.784003	0.006641
2492.393093	0.013781	401.220820	0.002218	5.391957	0.111350	0.917150	0.003291
3300.082320	0.038481	303.022744	0.003533	1.931123	0.111379	0.509763	0.009192
3522.773568	0.023308	283.867237	0.001878	3.187883	0.111387	0.130998	0.005569

Note: Periods and Period Errors are not outputted by Pyperiod, but are extrapolated from Frequencies and Frequency Errors

Table 10: TESS Sector 56 Pulsation Modes

Frequency (μHz)	Frequency Error	Period (seconds)	Period Error	Amplitude (ppt)	Amplitude Error	Phase (radian)	Phase Error
371.546884	0.007580	2691.450375	0.054907	2.071750	0.069140	0.453489	0.005414
417.710141	0.004930	2394.004605	0.028253	3.214947	0.069135	0.466949	0.003520
476.844777	0.008082	2097.118493	0.035542	1.930947	0.069135	0.001107	0.005772
1012.956357	0.007128	987.209363	0.006947	2.221949	0.069142	0.951754	0.005091
1111.790818	0.002235	899.449774	0.001808	9.185543	0.070277	0.485032	0.001606
1112.951527	0.007987	898.511728	0.006448	2.198787	0.070266	0.525149	0.005740
1151.507636	0.005472	868.426721	0.004127	2.931672	0.069152	0.802172	0.003908
1164.391954	0.003748	858.817339	0.002765	4.016293	0.069149	0.142351	0.002677
1210.469240	0.001777	826.125908	0.001213	8.592394	0.069137	0.901282	0.001270
1481.355797	0.008315	675.057270	0.003789	1.932246	0.069145	0.498480	0.005940
1522.858210	0.001630	656.659952	0.000703	9.455575	0.069185	0.133294	0.001164
1530.651475	0.003125	653.316589	0.001334	4.933622	0.069176	0.103271	0.002232
1628.166349	0.000958	614.187857	0.000361	16.087871	0.069147	0.172371	0.000684
1999.738250	0.002206	500.065446	0.000552	6.988517	0.069152	0.124850	0.001576
2223.863908	0.003689	449.667804	0.000746	2.532046	0.069148	0.091132	0.002636
2492.193481	0.006515	401.252956	0.001049	2.385141	0.069183	0.358920	0.004656
2502.277035	0.006822	399.636006	0.001089	2.352638	0.069178	0.513143	0.004875
3151.017958	0.008319	317.357760	0.000838	1.951784	0.069175	0.727715	0.005947
3522.789112	0.008332	283.865985	0.000671	1.911327	0.069189	0.571854	0.005958

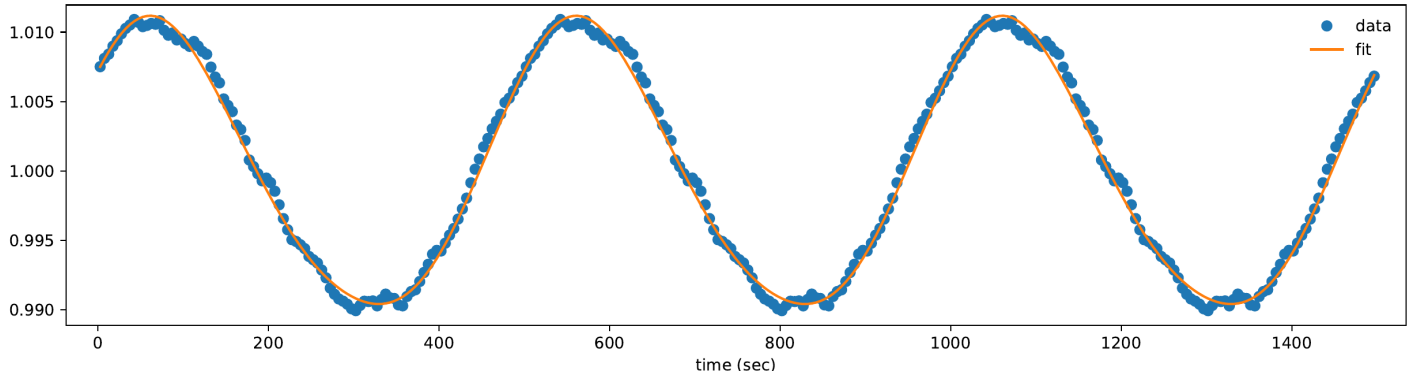
Note: Periods and Period Errors are not outputted by Pyperiod, but are extrapolated from Frequencies and Frequency Errors

B Folded Lightcurve Fits

All lightcurve fits are for TESS Sector 42 only.

B.1 Firsthalf fit: 499.676444 $\ell = 2$: $m = 0$

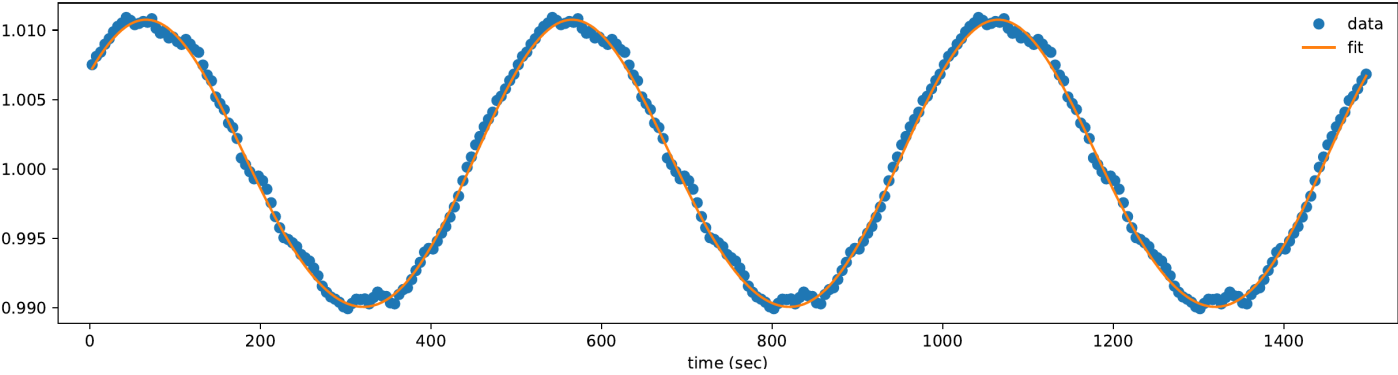
Res2	tau	theta.i	N			
3.10676115e-07	175.486 +/- 0.005 s	89.9853 +/- 0.0023 deg	15.000 +/- 0.003			
Amp	Amp_err	Period	Phase	Phase_err	l	m
0.25503	0.00001	499.676444	-2.84262	0.00008	2	0



B.2 Firsthalf fit: 499.676444 $\ell = 2$: $m = 1$

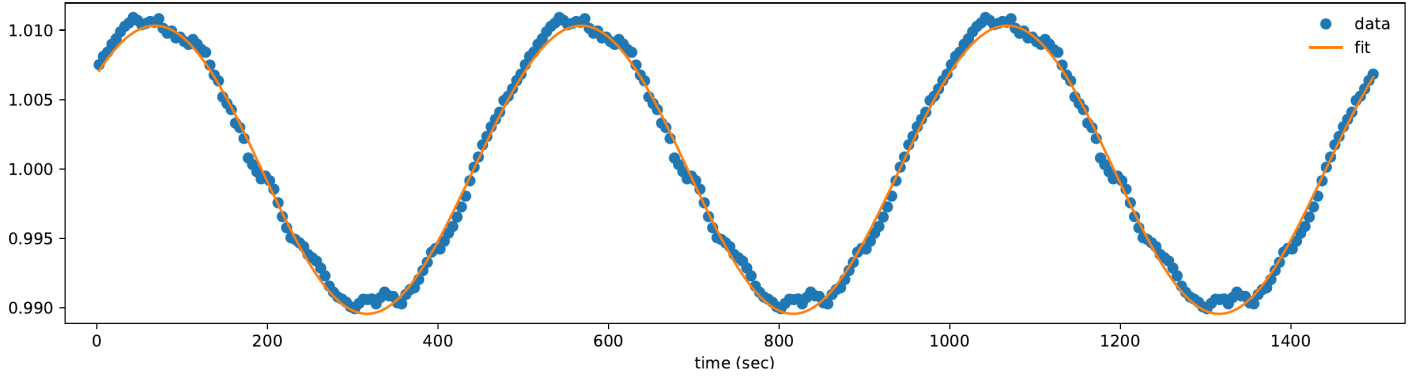
Res2	tau	theta_i	N			
2.00776182e-07	169.786 +/- 0.056 s	48.6788 +/- 0.0294 deg	33.266 +/- 0.042			

Amp	Amp_err	Period	Phase	Phase_err	l	m
0.21804	0.00006	499.676444	-2.85939	0.00030	2	1



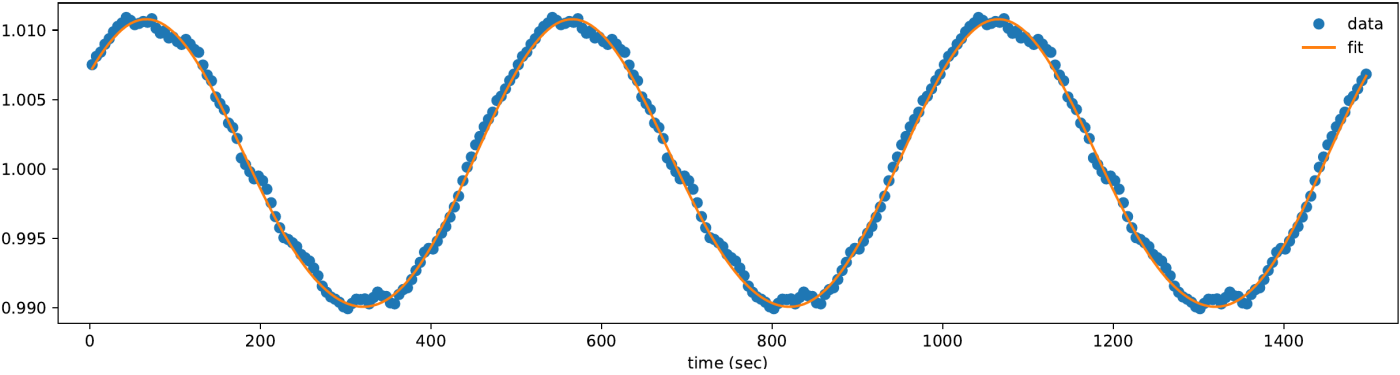
B.3 Firsthalf fit: 499.676444 $\ell = 2$: $m = 2$

Res2	tau	theta_i	N			
3.35540100e-07	190.549 +/- 0.013 s	89.9690 +/- 0.0042 deg	15.000 +/- 0.024			
Amp	Amp_err	Period	Phase	Phase_err	l	m
0.22624	0.00002	499.676444	0.32901	0.00006	2	2



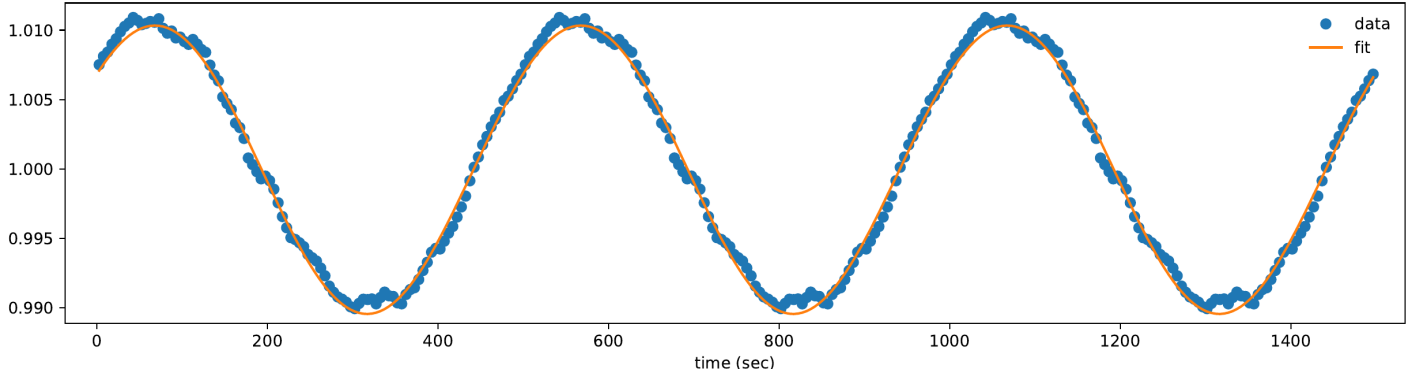
B.4 Firsthalf fit: 499.676444 $\ell = 2$: $m = -1$

Res2	tau	theta_i	N			
2.04253805e-07	189.896 +/- 0.007 s	41.6193 +/- 0.0504 deg	45.422 +/- 0.008			
Amp	Amp_err	Period	Phase	Phase_err	l	m
0.24664	0.00011	499.676444	0.31280	0.00007	2	-1



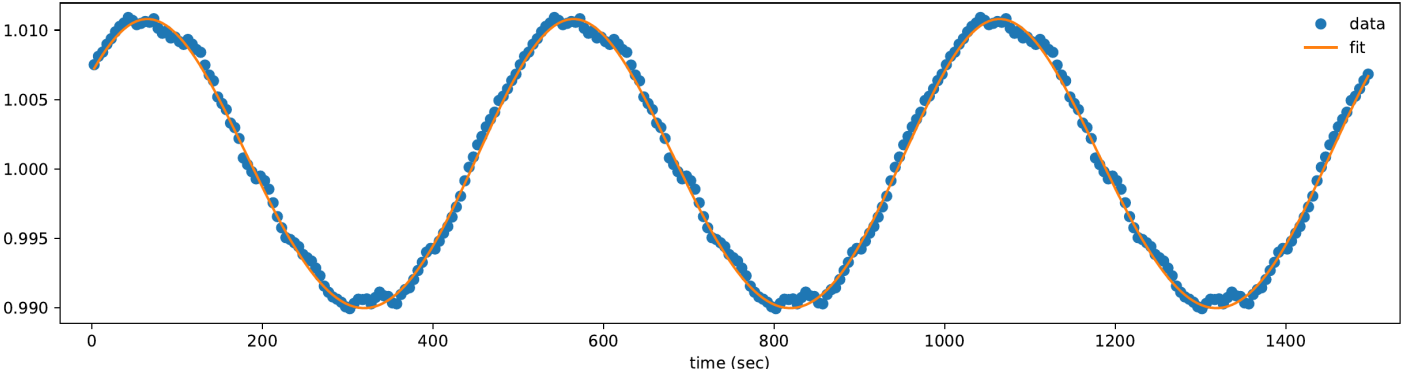
B.5 Firsthalf fit: 499.676444 $\ell = 2$: $m = -2$

Res2	tau	theta_i	N			
3.35305913e-07	198.774 +/- 0.012 s	89.7909 +/- 0.0044 deg	15.000 +/- 0.007			
Amp	Amp_err	Period	Phase	Phase_err	l	m
0.23486	0.00002	499.676444	0.34363	0.00057	2	-2



B.6 Firsthalf fit: 499.676444 $\ell = 1$: $m = 0$

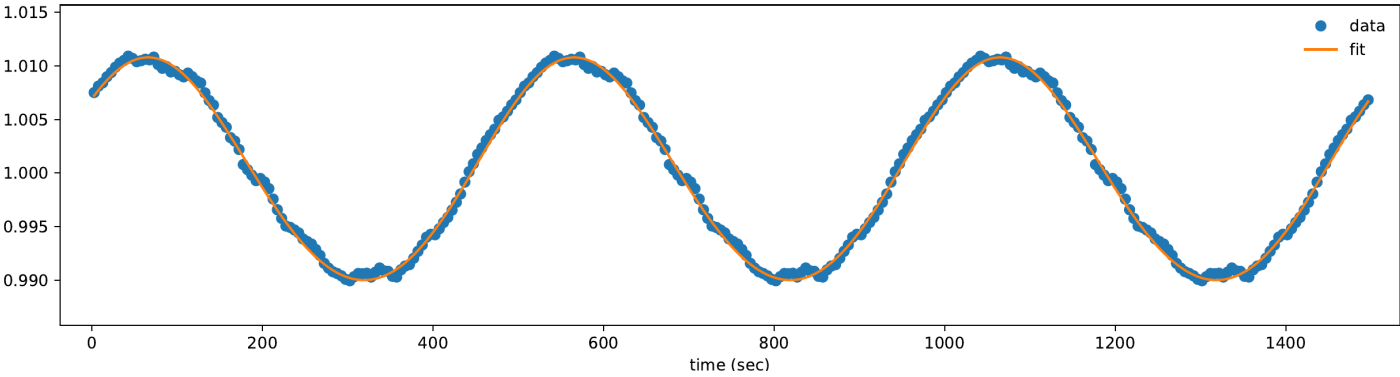
Res2	tau	theta_i	N			
2.10900403e-07	202.235 +/- 0.005 s	46.0017 +/- 0.0046 deg	20.957 +/- 0.013			
Amp	Amp_err	Period	Phase	Phase_err	l	m
0.11276	0.00002	499.676444	0.35040	0.00011	1	0



B.7 Firsthalf fit: 499.676444 $\ell = 1$: $m = 1$

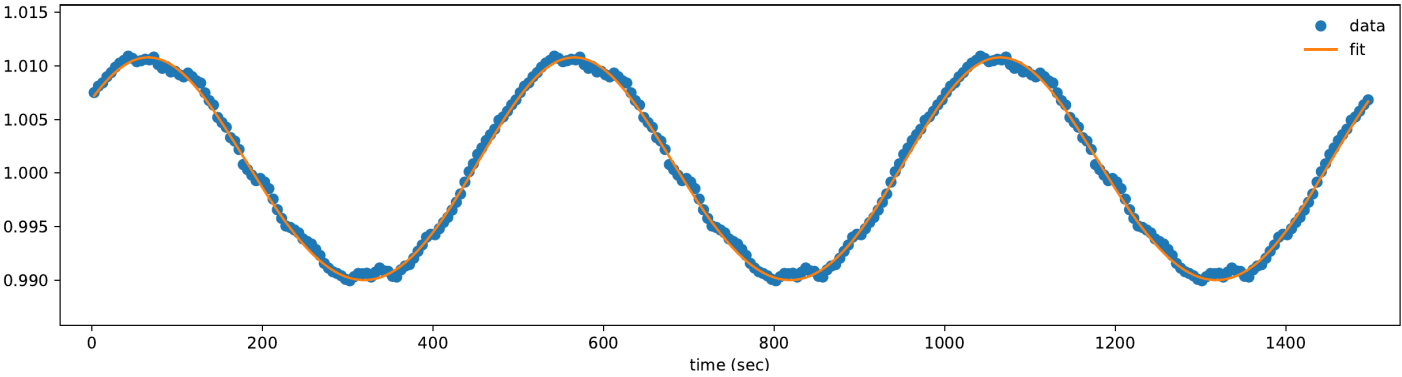
Res2	tau	theta_i	N			
2.11338891e-07	186.950 +/- 0.020 s	62.3897 +/- 0.0065 deg	41.882 +/- 0.190			

Amp	Amp_err	Period	Phase	Phase_err	l	m
0.11846	0.00002	499.676444	-2.82152	0.00005	1	1



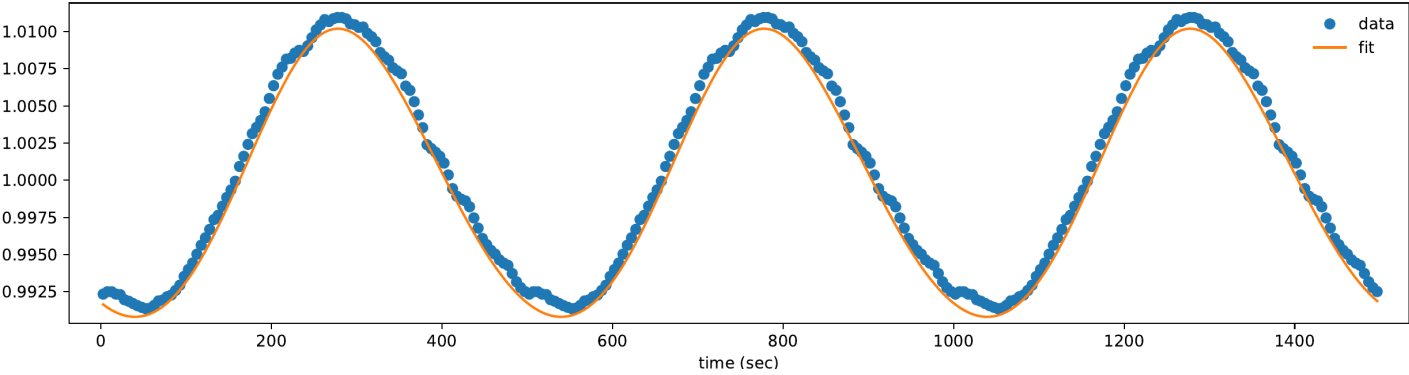
B.8 Firsthalf fit: 499.676444 $\ell = 1$: $m = -1$

Res2	tau	theta_i	N			
2.13163788e-07	203.997 +/- 0.006 s	49.9459 +/- 0.0424 deg	41.608 +/- 0.036			
Amp	Amp_err	Period	Phase	Phase_err	l	m
0.14827	0.00008	499.676444	0.34979	0.00020	1	-1



B.9 Secondhalf fit: 499.735414 $\ell = 1$: $m = 0$

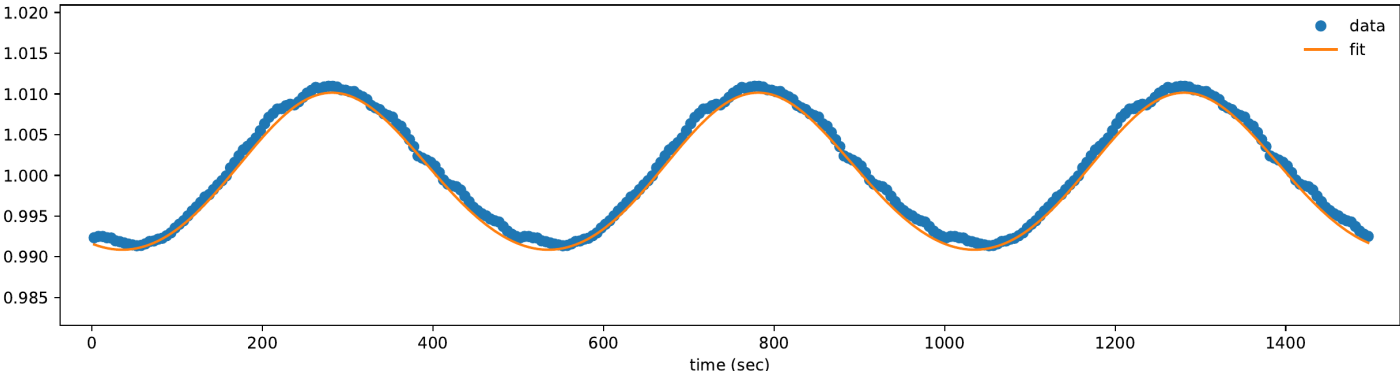
Res2	tau	theta_i	N			
6.94512963e-07	166.706 +/- 0.613 s	71.0582 +/- 0.2287 deg	15.000 +/- 0.286			
Amp	Amp_err	Period	Phase	Phase_err	l	m
0.18979	0.00142	499.735414	-2.43485	0.00158	1	0



B.10 Secondhalf fit: 499.735414 $\ell = 1$: $m = 1$

Res2	tau	theta_i	N			
7.36109157e-07	232.820 +/- 0.014 s	48.5248 +/- 0.0082 deg	57.303 +/- 0.081			

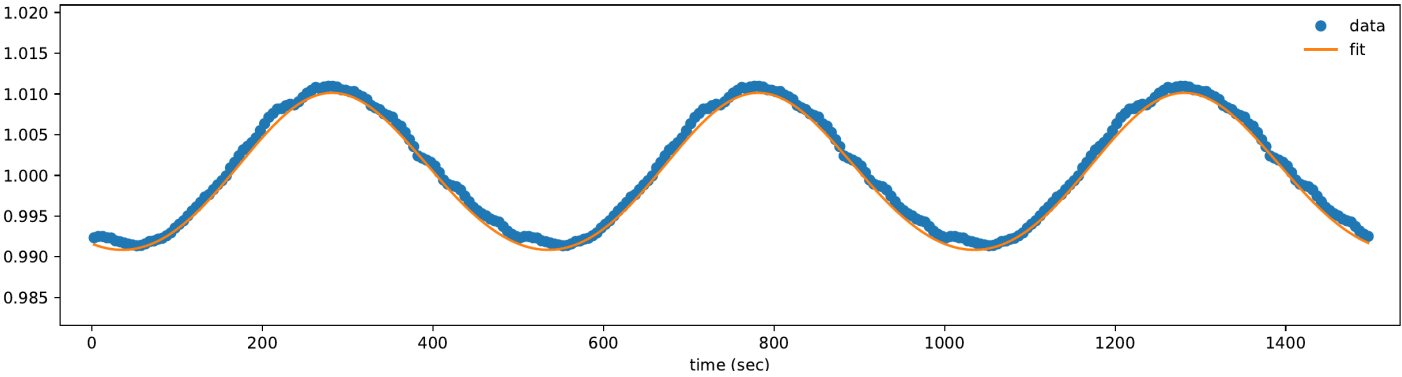
Amp	Amp_err	Period	Phase	Phase_err	l	m
0.15870	0.00001	499.735414	0.81655	0.00004	1	1



B.11 Secondhalf fit: 499.735414 $\ell = 1$: $m = -1$

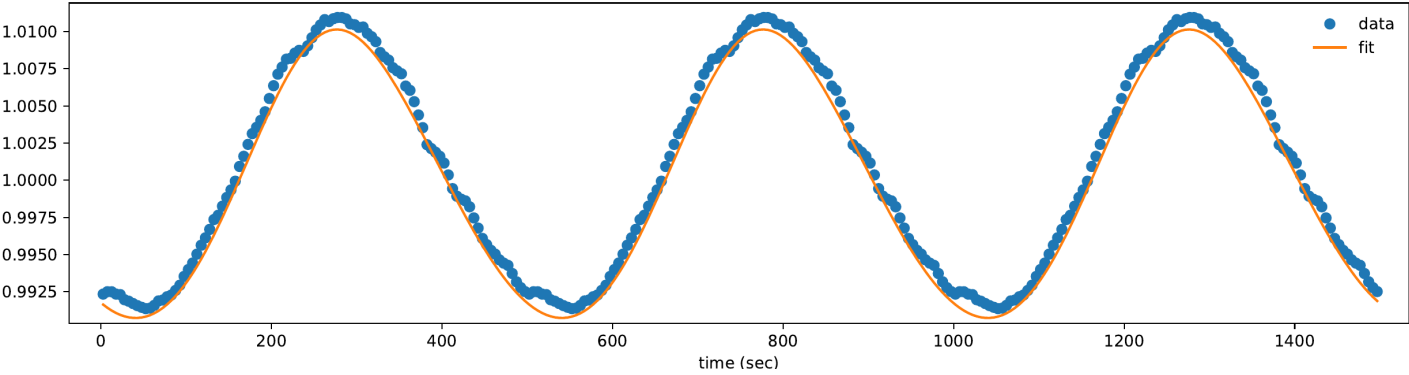
Res2	tau	theta_i	N			
7.36565151e-07	227.248 +/- 0.006 s	90.0000 +/- 0.0042 deg	55.447 +/- 0.079			

Amp	Amp_err	Period	Phase	Phase_err	l	m
0.11420	0.00001	499.735414	-2.32931	0.00010	1	-1



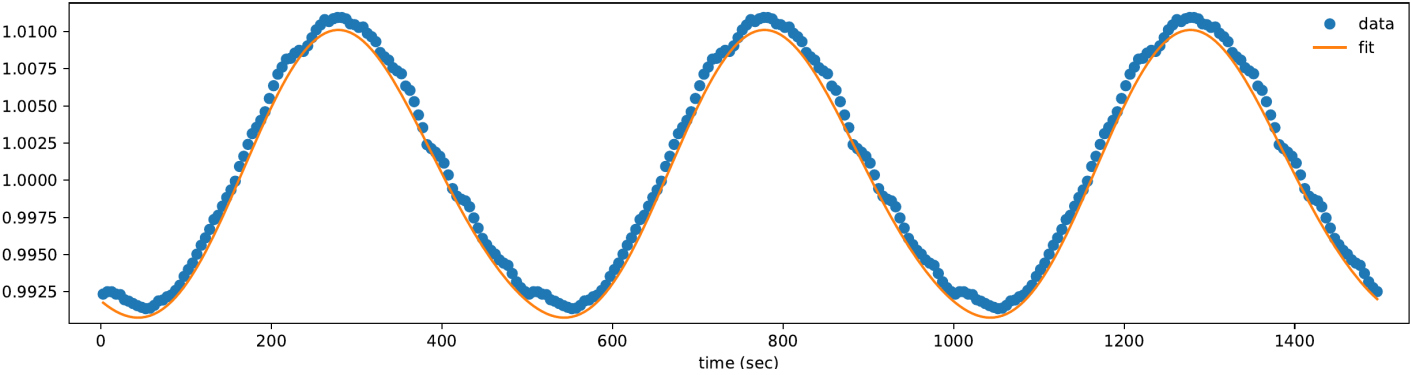
B.12 Secondhalf fit: 499.735414 $\ell = 2$: $m = 0$

Res2	tau	theta_i	N			
6.91904512e-07	129.252 +/- 0.117 s	22.1774 +/- 0.0330 deg	15.010 +/- 0.007			
Amp	Amp_err	Period	Phase	Phase_err	l	m
0.12150	0.00015	499.735414	-2.54110	0.00032	2	0



B.13 Secondhalf fit: 499.735414 $\ell = 2$: $m = 1$

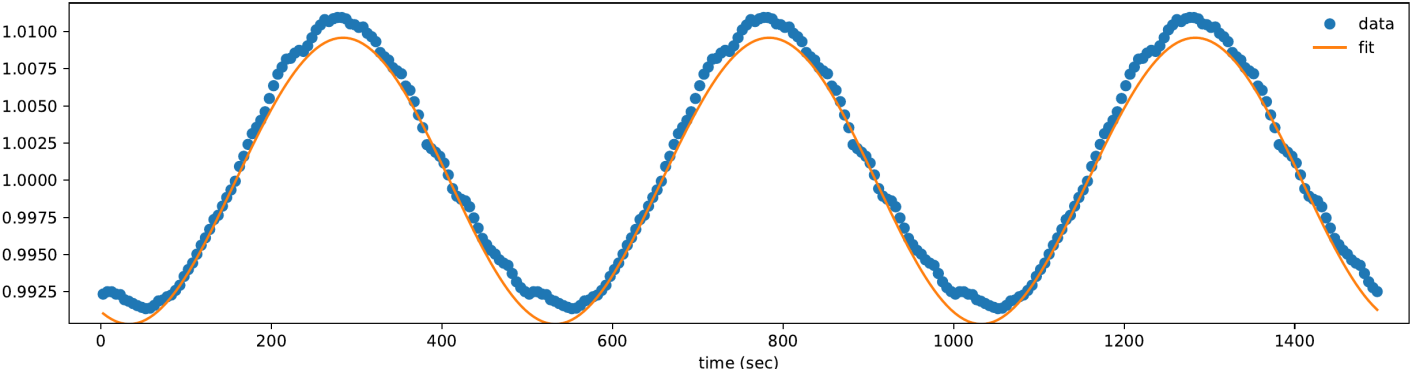
Res2	tau	theta_i	N			
6.75450141e-07	68.725 +/- 0.061 s	58.1748 +/- 0.0304 deg	33.642 +/- 0.011			
Amp	Amp_err	Period	Phase	Phase_err	l	m
0.12709	0.00008	499.735414	0.30497	0.00041	2	1



B.14 Secondhalf fit: 499.735414 $\ell = 2$: $m = 2$

Res2	tau	theta_i	N			
9.09648611e-07	178.023 +/- 0.014 s	78.4232 +/- 0.0047 deg	15.000 +/- 0.025			

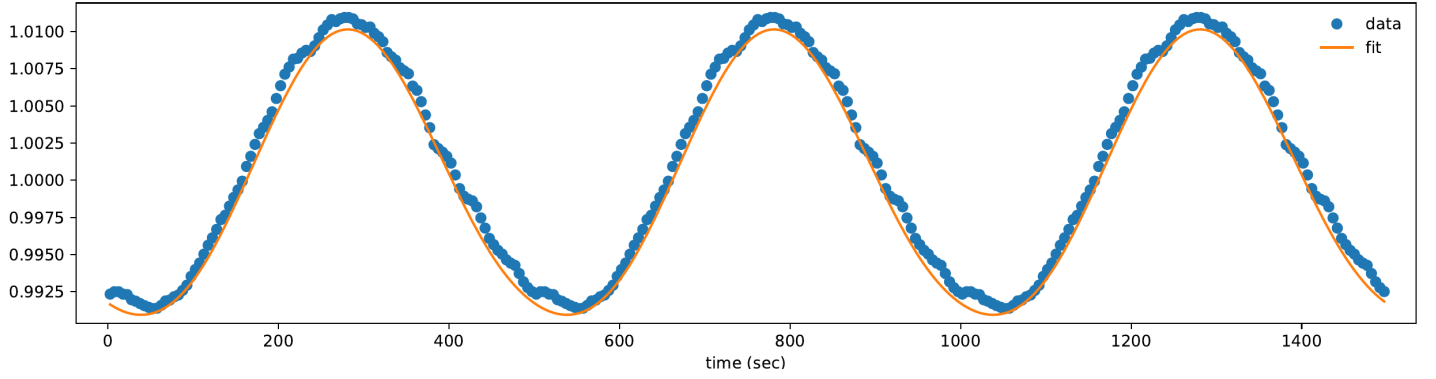
Amp	Amp_err	Period	Phase	Phase_err	l	m
0.21177	0.00001	499.735414	-2.41096	0.00020	2	2



B.15 Secondhalf fit: 499.735414 $\ell = 2$: $m = -1$

Res2	tau	theta_i	N			
7.15530718e-07	179.107 +/- 0.005 s	48.6134 +/- 0.0093 deg	45.870 +/- 0.006			

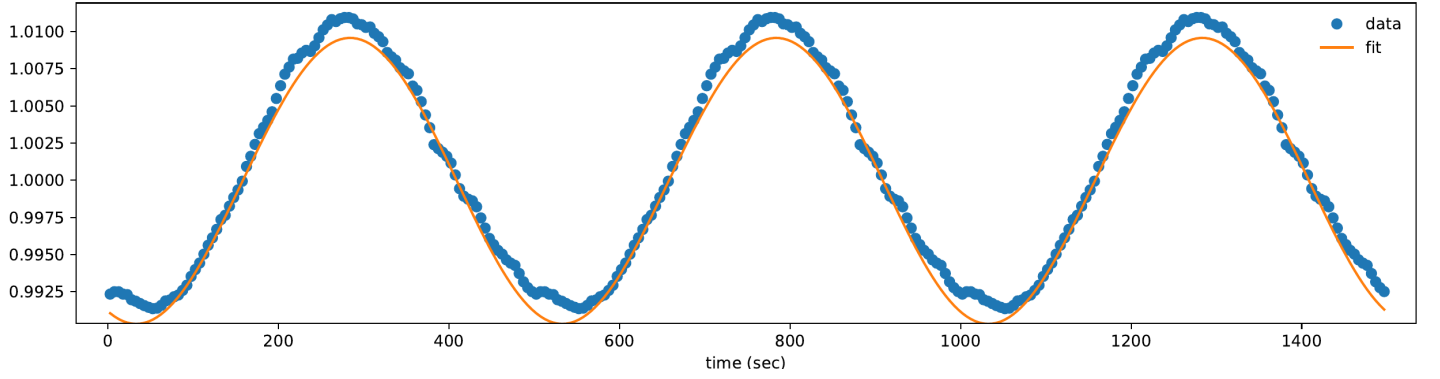
Amp	Amp_err	Period	Phase	Phase_err	l	m
0.21607	0.00001	499.735414	-2.42047	0.00005	2	-1



B.16 Secondhalf fit: 499.735414 $\ell = 2$: $m = -2$

Res2	tau	theta_i	N			
9.09522295e-07	179.860 +/- 0.018 s	76.7070 +/- 0.0802 deg	15.000 +/- 0.055			

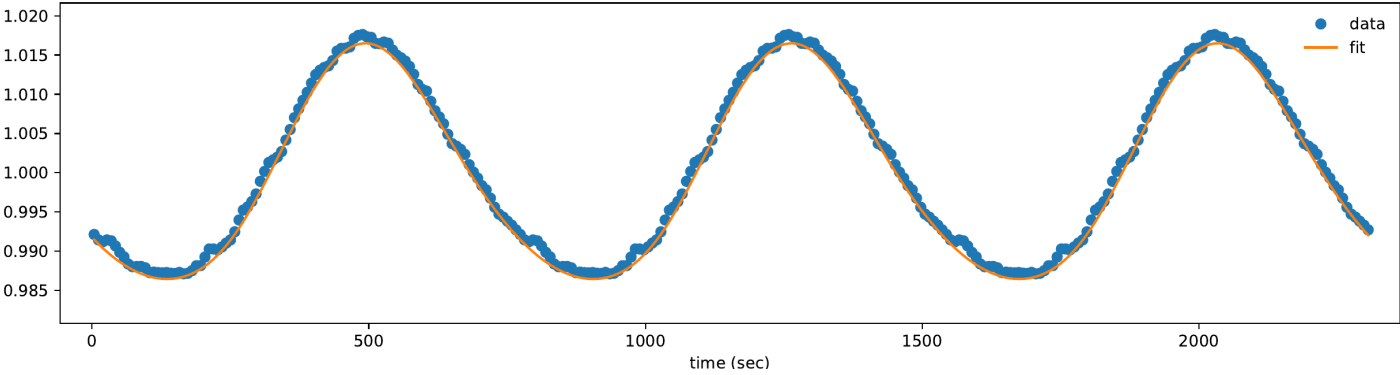
Amp	Amp_err	Period	Phase	Phase_err	l	m
0.21618	0.00014	499.735414	-2.40829	0.00008	2	-2



B.17 Secondhalf fit: 769.861399 $\ell = 1$: $m = 1$

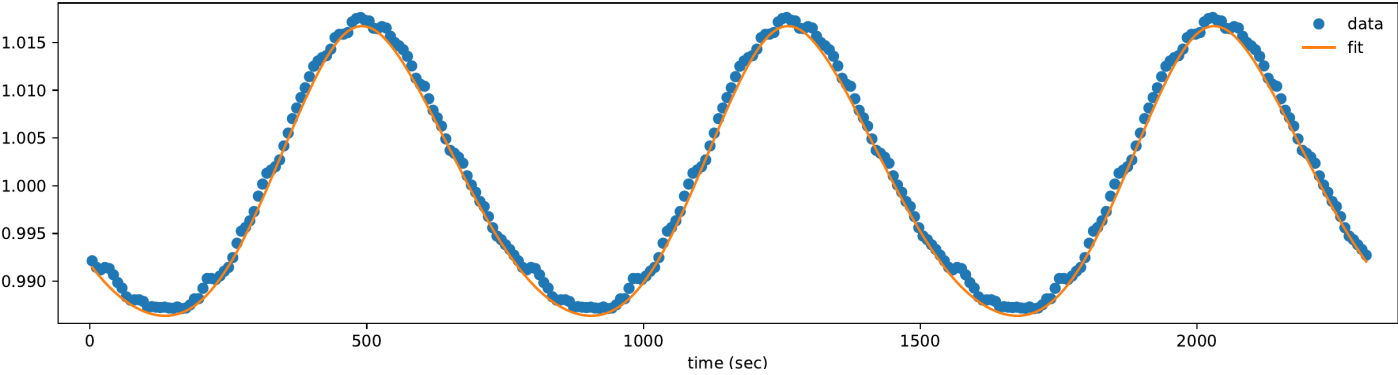
Res2	tau	theta_i	N			
7.67244260e-07	142.771 +/- 0.121 s	55.9276 +/- 0.0467 deg	89.818 +/- 0.228			

Amp	Amp_err	Period	Phase	Phase_err	l	m
0.12536	0.00015	769.861399	-0.10876	0.00024	1	1



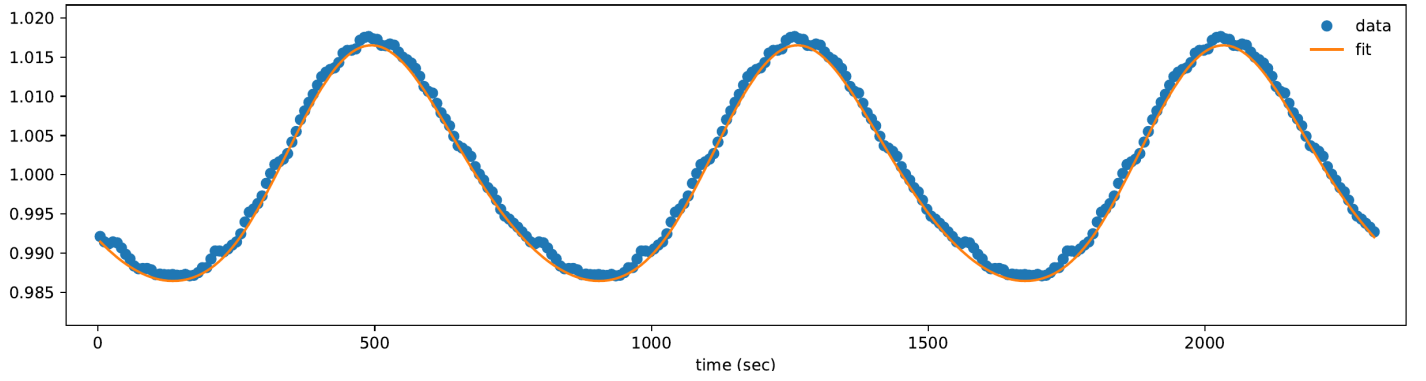
B.18 Secondhalf fit: 769.861399 $\ell = 1$: $m = 0$

Res2	tau	theta_i	N			
7.93872838e-07	286.633 +/- 0.509 s	71.3622 +/- 0.0371 deg	15.451 +/- 0.027			
Amp	Amp_err	Period	Phase	Phase_err	l	m
0.32849	0.00102	769.861399	-2.93656	0.00065	1	0



B.19 Secondhalf fit: 769.861399 $\ell = 1$: $m = -1$

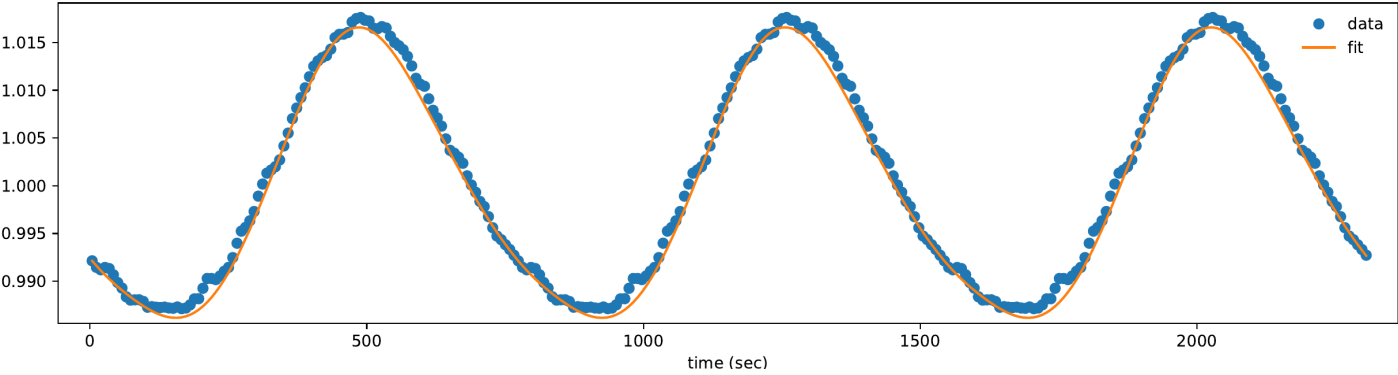
Res2	tau	theta_i	N			
7.67193502e-07	143.697 +/- 0.046 s	57.2276 +/- 0.0101 deg	89.019 +/- 0.024			
Amp	Amp_err	Period	Phase	Phase_err	l	m
0.12311	0.00002	769.861399	3.03510	0.00013	1	-1



B.20 Secondhalf fit: 769.861399 $\ell = 2$: $m = 0$

Res2	tau	theta_i	N			
9.81182826e-07	176.341 +/- 0.005 s	90.0000 +/- 0.0012 deg	15.000 +/- 0.003			

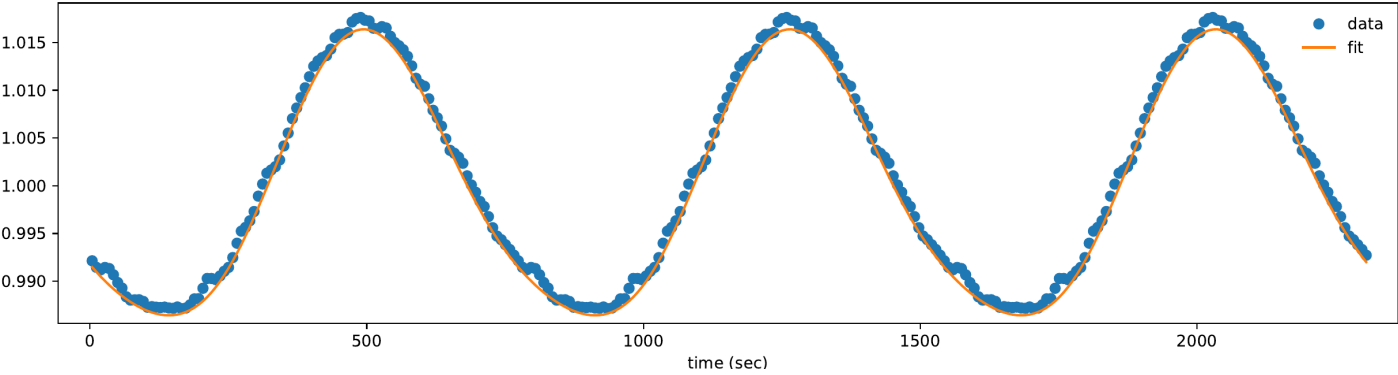
Amp	Amp_err	Period	Phase	Phase_err	l	m
0.26487	0.00002	769.861399	-0.00639	0.00004	2	0



B.21 Secondhalf fit: 769.861399 $\ell = 2$: $m = 1$

Res2	tau	theta_i	N			
7.64337526e-07	228.017 +/- 0.264 s	69.2112 +/- 0.0288 deg	17.749 +/- 0.029			

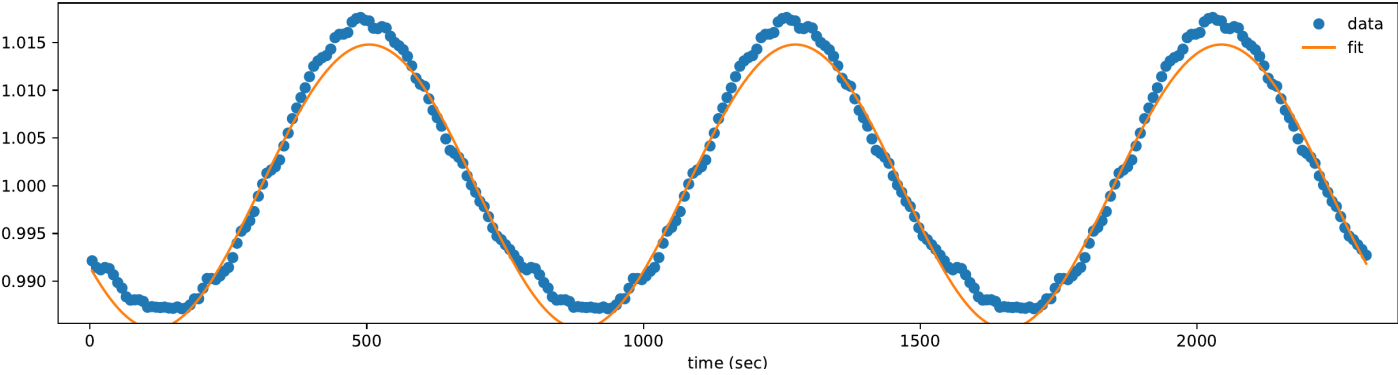
Amp	Amp_err	Period	Phase	Phase_err	l	m
0.41676	0.00074	769.861399	0.11918	0.00051	2	1



B.22 Secondhalf fit: 769.861399 $\ell = 2$: $m = 2$

Res2	tau	theta_i	N			
2.45939591e-06	185.108 +/- 0.045 s	90.0000 +/- 0.0042 deg	15.000 +/- 0.084			

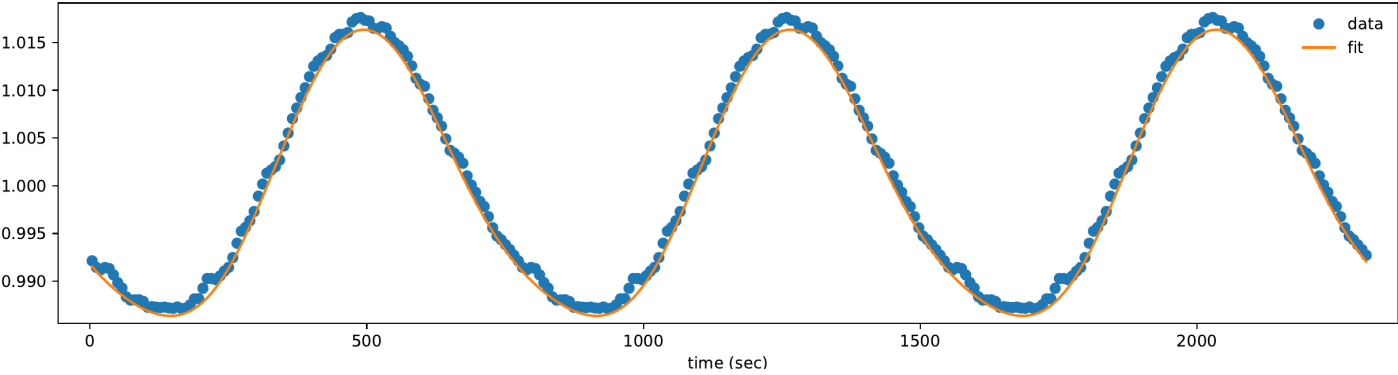
Amp	Amp_err	Period	Phase	Phase_err	l	m
0.22680	0.00058	769.861399	-3.11417	0.00123	2	2



B.23 Secondhalf fit: 769.861399 $\ell = 2$: $m = -1$

Res2	tau	theta_i	N			
7.69169178e-07	175.541 +/- 0.018 s	62.3346 +/- 0.0316 deg	27.003 +/- 0.060			

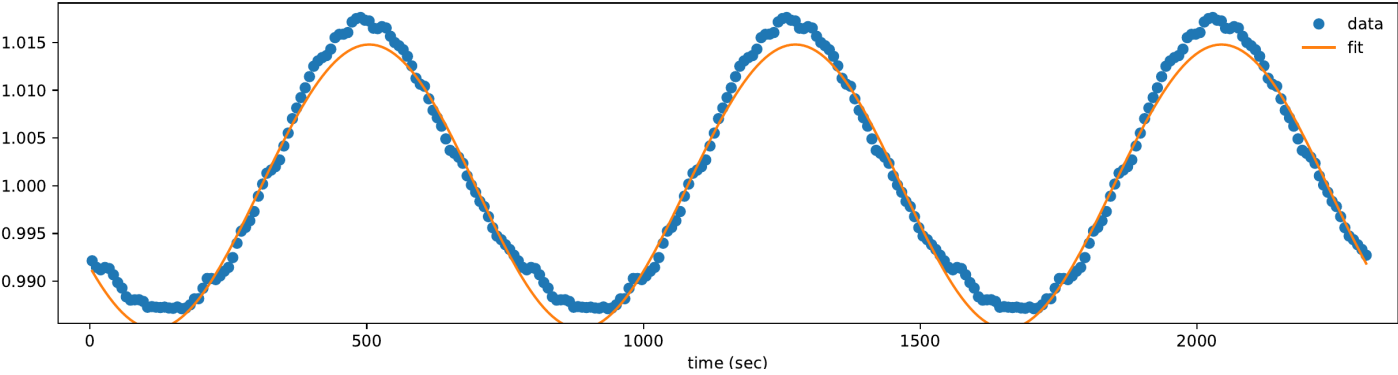
Amp	Amp_err	Period	Phase	Phase_err	l	m
0.29185	0.00012	769.861399	-3.13993	0.00005	2	-1



B.24 Secondhalf fit: 769.861399 $\ell = 2$: $m = -2$

Res2	tau	theta_i	N			
2.45939230e-06	185.081 +/- 0.640 s	90.0000 +/- 0.0042 deg	15.000 +/- 47.478			

Amp	Amp_err	Period	Phase	Phase_err	l	m
0.22676	0.00800	769.861399	-3.11433	0.53922	2	-2



C Firsthalf Lightcurve Fit

Note the low N value of this fit. While it is correctly modelling the lightcurve, changes need to be made to ensure the N parameters are correct. We would expect a much higher N for G 29-38. This problem continues in Appendix D.

Table 11

Res2	tau	theta.i	N
3.37661616e-04	339.735 +/- 0.039 s	40.2266 +/- 0.0047 deg	15.000 +/- 0.007

Amp	Amp_err	Period	Phase	Phase_err	ℓ	m
0.15335	0.00002	401.225904	-0.36524	0.00050	1	1
0.43489	0.00005	499.676444	-2.69928	0.00016	2	1
0.33047	0.00011	503.262982	2.64689	0.00050	2	2
0.03269	0.00002	611.995832	0.99089	0.00138	1	1
0.07302	0.00002	610.64502	2.92723	0.00051	1	0
0.05631	0.00003	608.870244	1.89139	0.00049	1	-1
0.07053	0.00002	654.970932	2.71146	0.00053	1	0
0.10817	0.00005	653.480618	3.11105	0.00043	1	-1
0.06177	0.00002	569.444758	-0.23507	0.00051	1	-1
0.28362	0.00003	764.86033	-1.96836	0.00040	2	-2
0.14160	0.00003	773.559599	-0.19534	0.00045	2	0
0.19180	0.00002	770.422624	1.40457	0.00029	2	-1
0.06967	0.00002	812.532444	1.24620	0.00046	2	-1

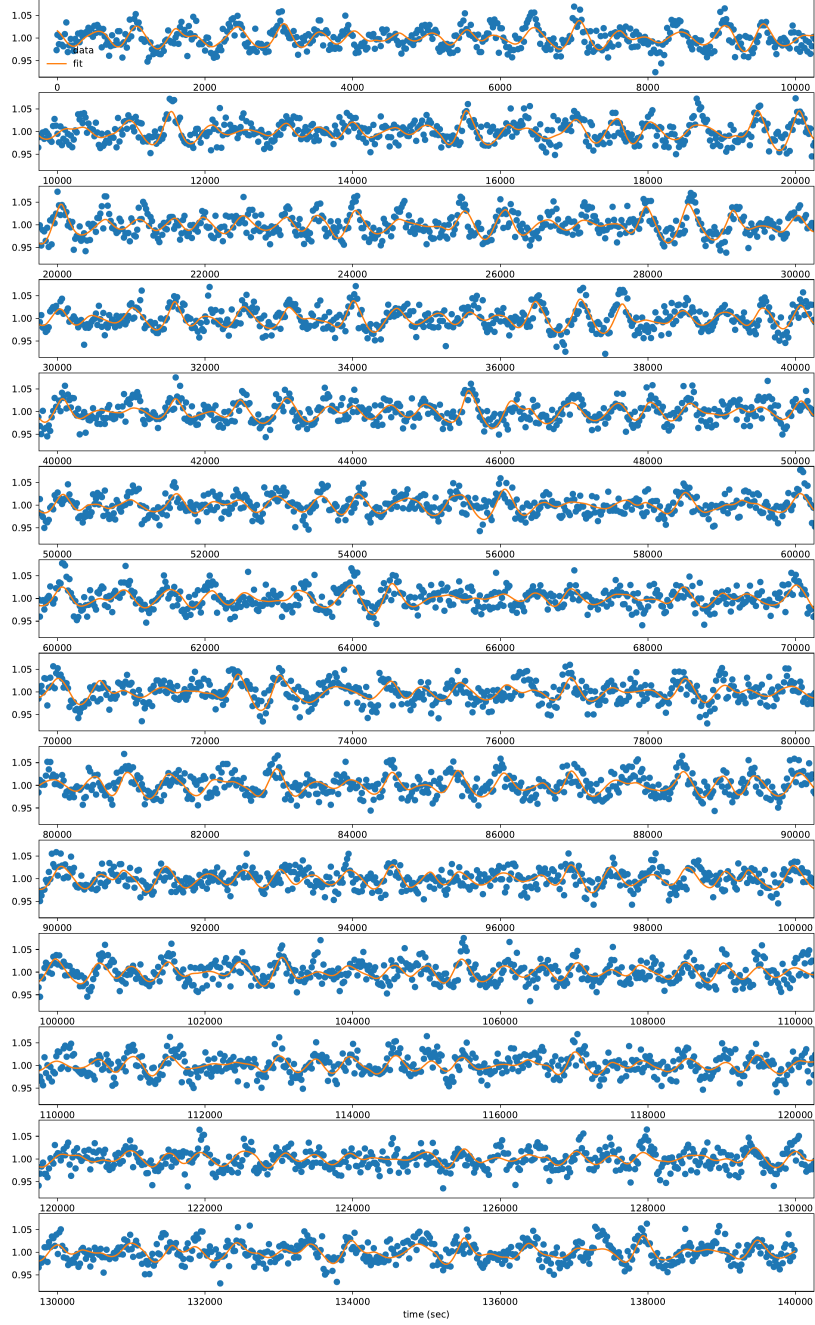


Figure 17

D Secondhalf Lightcurve Fit

Here the code is dropping the last mode (903 second period) to an amplitude of 0. Again, this is incorrect and needs to be adjusted for future work.

Table 12

Res2	tau	theta.i	N
3.69622062e-04	251.374 +/- 0.023 s	71.5009 +/- 0.0039 deg	15.000 +/- 0.007

Amp	Amp_err	Period	Phase	Phase_err	ℓ	m
0.09508	0.00002	401.22082	-2.56543	0.00047	1	1
0.30329	0.00004	499.737949	-2.60178	0.00043	2	-1
0.03632	0.00002	569.435942	-2.28179	0.00047	1	-1
0.03247	0.00002	608.882486	-0.44581	0.00053	1	-1
0.09080	0.00002	610.656128	2.13476	0.00056	1	0
0.06900	0.00002	612.080711	-0.45414	0.00049	1	1
0.04607	0.00002	653.461876	-1.50190	0.00103	1	-1
0.09961	0.00002	655.004966	2.58322	0.00074	1	0
0.44061	0.00005	769.843357	-2.69475	0.00014	2	-1
0.42828	0.00005	773.713584	-2.06497	0.00027	2	0
0.10980	0.00002	811.092831	1.56285	0.00059	2	-1
0.00000	0.00001	903.434371	1.29897	0.00088	1	1

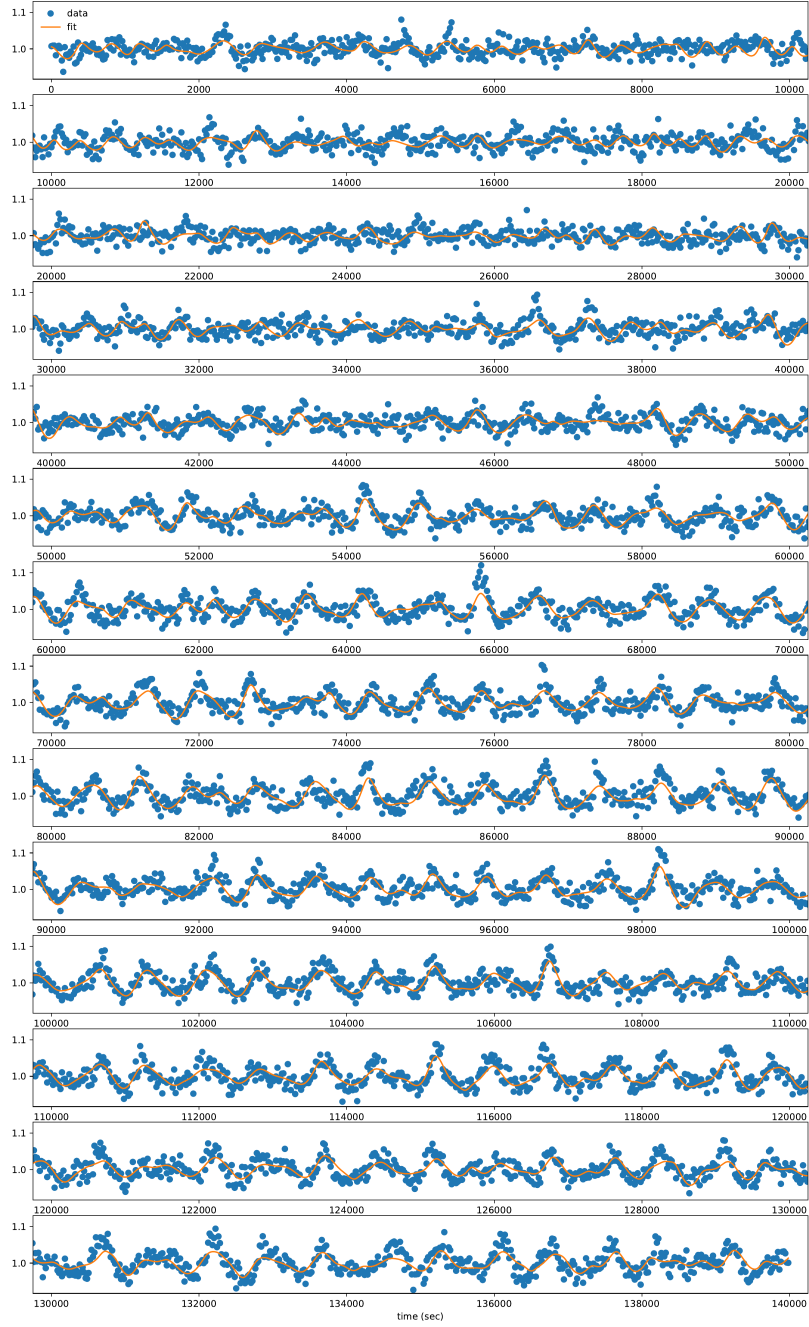


Figure 18